Biophysical Journal Volume 93 August 2007 709–728

A Kinetic Model for Calcium Dynamics in RAW 264.7 Cells: 1. Mechanisms, Parameters, and Subpopulational Variability

Mano Ram Maurya* and Shankar Subramaniam*†‡

*Department of Bioengineering; †Department of Chemistry and Biochemistry; and ‡Graduate Program in Bioinformatics, University of California, San Diego, California

ABSTRACT Calcium (Ca^{2+}) is an important second messenger and has been the subject of numerous experimental measurements and mechanistic studies in intracellular signaling. Calcium profile can also serve as a useful cellular phenotype. Kinetic models of calcium dynamics provide quantitative insights into the calcium signaling networks. We report here the development of a complex kinetic model for calcium dynamics in RAW 264.7 cells stimulated by the C5a ligand. The model is developed using the vast number of measurements of in vivo calcium dynamics carried out in the Alliance for Cellular Signaling (AfCS) Laboratories. Ligand binding, phospholipase C-β (PLC-β) activation, inositol 1,4,5-trisphosphate (IP_3) receptor (IP_3R) dynamics, and calcium exchange with mitochondria and extracellular matrix have all been incorporated into the model. The experimental data include data from both native and knockdown cell lines. Subpopulational variability in measurements is addressed by allowing nonkinetic parameters to vary across datasets. The model predicts temporal response of Ca^{2+} concentration for various doses of C5a under different initial conditions. The optimized parameters for IP_3R dynamics are in agreement with the legacy data. Further, the half-maximal effect concentration of C5a and the predicted dose response are comparable to those seen in AfCS measurements. Sensitivity analysis shows that the model is robust to parametric perturbations.

INTRODUCTION

Cytosolic calcium is a second messenger and plays an important role in intracellular signaling (1). Cytosolic Ca^{2+} is involved in regulating numerous cellular functions by regulating the activity of proteins such as calmodulin (2), calreticulin (3–5), and calcineurin (6). Dynamic changes in intracellular calcium serve both as an important indicator of cellular events and a quantitative measure of cellular response to stimuli.

Basic mechanism of calcium dynamics

In a eukaryotic cell, the average cytosolic Ca^{2+} concentration ($[Ca^{2+}]_i$) is maintained low (0.05–0.5 μM), whereas Ca^{2+} concentrations in extracellular space and endoplasmic (or sarcoplasmic) reticulum (ER/SR) ($[Ca^{2+}]_{ER}$) are several thousands times higher (7). This large concentration gradient of Ca^{2+} between different cellular compartments is utilized by cells to generate rapid intracellular Ca^{2+} changes through receptor-mediated mechanisms. In nonexcitable cells, such as macrophages, ligand-induced release of calcium from the ER is the main initiator of calcium dynamics. In excitable cells, other sources that initiate dynamics include the calcium influx through voltage-gated channels on the plasma membrane (PM) (8–11). Both these eventually lead to increased activation and opening of the inositol 1,4,5-trisphosphate (IP_3) receptor (IP_3R) channels on the ER membrane through either increased hydrolysis of phosphatidylinositol 4,5-bisphosphate (PIP_2) into IP_3 (12–14) or local increase in $[Ca^{2+}]_i$ leading to calcium-induced calcium release (CICR) (15–17). Calcium release from the ER leads to increased Ca^{2+} in the cytosol. Most of the calcium released binds to various proteins, such as calmodulin (CaM). Calcium is also pumped back to the ER by the sarco(endo)plasmic reticulum calcium ATPase (SERCA) pump. Some calcium is also expelled to the extracellular space through an Na^+/Ca^{2+} exchanger (NCX) and the plasma membrane calcium ATPase (PMCA) pump. Calcium exchange with the mitochondria also has been observed at elevated levels of $[Ca^{2+}]_i$. If Ca^{2+} concentration in the ER becomes quite low, calcium can enter the cell as calcium-release-activated current (CRAC) through store-operated channels (SOC) on the plasma membrane (18–20). Finally, calcium response can propagate to nearby cells connected through gap-junctions resulting in calcium waves (20).

Variation across different cell types

Cytosolic Ca^{2+} can be measured relatively easily using fluorescence and dye-based methods (21,22) at high sample rates (one sample every few seconds) (23). Recent reviews by Van Den Brink et al. (21) and Takahashi et al. (22) deal with elaborate descriptions of various methods of measuring free $[Ca^{2+}]$ and calcium fluxes between various compartments, such as the cytosol, the ER, and the mitochondria. Calcium levels can vary substantially from one cell type to another. For example, in excitable cells such as neuronal cells and muscle cells, for which most calcium models and measurement techniques have been developed (13,21,24–28), basal $[Ca^{2+}]_i$

Submitted September 13, 2006, and accepted for publication February 27, 2007.

Address reprint requests to Shankar Subramaniam, Dept. of Bioengineering, University of California, San Diego, 9500 Gilman Dr., La Jolla, CA 92093-0412. Tel.: 858-822-0986; Fax: 858-822-5722; E-mail: shankar@ucsd.edu.

Editor: Ian Parker.

0006-3495/07/08/709/20 $2.00

doi: 10.1529/biophysj.106.097469

is in the 0.2–0.5 μM range, whereas in nonexcitable cells such as macrophages, including RAW 264.7 cells (29,30), it is between 0.03 and 0.1 μM. In macrophages, due to their nonexcitable nature, oscillations are generally not observed, as evidenced by the Alliance for Cellular Signaling (AfCS) calcium data (29) and discussed in (30–32). In fact, the maximal changes in $[Ca^{2+}]_i$ (spatially averaged) are also only $\sim$0.05–0.1 μM, except when cells are treated with strong activators such as the bacterial toxin lipopolysaccharide (30).

The need for a model for calcium dynamics in RAW 264.7 cells

Recently, AfCS has conducted a large array of experiments to measure the temporal response of cytosolic calcium in RAW 264.7 cells in response to various ligands. RAW 264.7 cells are a macrophage-like, Abelson leukemia virus transformed cell line derived from BALB/c mice (AfCS protocol PP00000226 (23,33)). Considering the importance of calcium signaling, substantial efforts have been devoted to develop mathematical models for calcium dynamics. However, much of the work has focused on excitable cells, such as neuronal cells (13,27) and muscle cells (10,11,21,24–26,28), in which calcium oscillations are prevalent. Recent efforts have also focused on nonexcitable cells (12,13,34). Although literature is replete with simple, as well as complex, models of calcium signaling, including those by Fink et al. (35), Mishra and Bhalla (13), and Lemon et al. (12), there are no models of calcium dynamics in RAW 264.7 cells in the published literature. The model presented by Mishra and Bhalla (13), which incorporates the mechanisms for G-protein signaling, IP_3R channels, IP_3 metabolism, and binding of calcium with many proteins such as calmodulin, is the most comprehensive detailed kinetic model for mammalian cells. Most of the parameters used for simulation of the model are taken from the literature and are robust for making qualitative comparisons for various cell types. However, these parameter values may not be able to capture the fine quantitative features of data for a given cell type. In fact, a comparison of the time course predicted by Lemon et al. (12) for a nonspecific cell type and by Fink et al. (35) for neuronal cells with the time course in AfCS experiments reveals that the effective time constant in AfCS data for the rise phase is several times larger than in Lemon et al. (12) and Fink et al. (35), whereas the decay phase is more gradual than in Fink et al. (35) and much faster than in Lemon et al. (12). Although precise quantitative comparisons/predictions of features such as peak height are not mandated from calculations, it is essential to capture overall temporal variations for a model to be accurate and predictive for describing calcium dynamics. Thus, there is a clear need for some cell-specific constraining of the parameters. One way to carry out constraining of the parameters is to tweak each parameter in a trial-and-error fashion. The alternative and arguably the best way is to use cell-specific in vivo data to develop a systems-level model. The known biochemistry and other constraints from legacy data must be included to maintain the qualitative generality of the results. RAW 264.7 cells are different from other cells such as muscle cells not only in size but also in the basal level of $[Ca^{2+}]_i$, as stated earlier. Further, AfCS experiments have shown that calcium response in RAW cells is nonoscillatory and exhibits just one peak after applying a ligand. Thus, it is reasonable to expect differences in the values of some of the lumped/effective kinetic parameters besides differences in the species concentrations in various cell types. Cell-specific modeling of calcium signaling, including the estimation/measurement of parameters, is quite important for real-life applications such as drug-dose response, and applications of systems biology. Also, in systemic models that include many processes and parameters, many different parameter ranges can yield different qualitative responses. Hence, even if one is interested in only qualitative results, some constraining of the parameters using cell-specific data is desired.

Recent AfCS experiments have revealed a new and very challenging problem. Different cell populations (cloned from the same parent cell), when triggered by a stimulus of the same strength, result in quantitatively as well as qualitatively different responses (different peak heights, rise times, etc.). According to our current understanding, the underlying cause is the variation in the unmeasurable concentrations of hundreds of species (components) inside the cells. This variability could be due to intrinsic sources, such as noise in gene expression (36), as well as extrinsic noise, such as unsynchronized cell cycles in different experiments. Though some of these fluctuations across cells get averaged out in cell populations, a nontrivial variation is still observed from one population to another. This variation is observed even in the basal levels in unstimulated and stimulated control cell lines and in knockdown cell lines, in addition to the variability after stimulation with ligands. If the basal levels were similar across different subpopulations (datasets), a common set of parameter values could have been used and then a knockdown could be modeled by modifying the parameter related to the knockdown process, e.g., the concentration of the relevant protein. The substantial ''subpopulational variability'' in the basal level required us to employ a special modeling approach in which some parameters are allowed to vary across different datasets. The AfCS data also includes a large set of perturbation data on the knockdown of proteins affecting the temporal characteristics of calcium dynamics. This data has been used for both modeling and validation of our context-specific models. The ligand used in this study is the complement 5a (C5a), a potent mediator of inflammation (37–44). An ordinary differential equation-based model is developed to understand calcium dynamics in RAW264.7 cells.

The first part of this two-part article deals with the development of a kinetic model using the AfCS data exhibiting subpopulational variability and prediction of dose response of C5a. Part 2 deals with the prediction of knockdown response and long-term response using the model developed in this article. Our modeling approach allowed us to utilize in vivo data exhibiting variability across different subpopulations. The resulting model elucidates the central role of phospholipase C (PLC) β (PLCβ) and IP_3 for calcium dynamics. Using the model, the efficacy of C5a is characterized and the robustness of calcium response is analyzed using global sensitivity analysis.

MATERIALS AND METHODS

Experimental data

We have utilized the time-course data on $[Ca^{2+}]_i$ response in macrophage RAW 264.7 cell populations made available by the AfCS (45). Owing to limitations of space, we refer to the AfCS website for the necessary details pertaining to experimental data (45). In brief, free $[Ca^{2+}]_i$ is measured using the Ca^{2+}-sensitive fluorescent dye fura-2 (AfCS protocol PP00000211 (23)). As described on the AfCS Web site (23) and in the literature (46,47), free $[Ca^{2+}]_i$ is computed from the ratio of the intensities of fluorescent light at two wavelengths (340 nm and 380 nm). The intensities are actually related to the amount of calcium-bound fura-2. However, using the rapid buffering approximation for fura-2, as well as other buffers present in the cytosol, it is possible to back out free $[Ca^{2+}]_i$ from the intensity measurements. In the Results section, we show that the rapid buffering approximation is valid, i.e., for a small perturbation in $[Ca^{2+}]_i$, the new equilibrated free $[Ca^{2+}]_i$ is reached much earlier than the next measurement. We use data from native cells as well as from knockdown cell lines. The knockdowns were carried out using short hairpin RNA interference (shRNAi). Data from four time-courses are used for constraining/estimating the parameters. Additional description of the data used is given in Supplementary Material (Preprocessing of time-course data).

Mathematical model of calcium dynamics in RAW 264.7 cells

A simplified model for calcium signaling that incorporates most of the mechanisms included in the existing models has been developed (Fig. 1). This simple model, however, includes several mechanisms explicitly so that knockdown of important proteins, such as G-protein-coupled receptor (GPCR) kinase (GRK), Arrestin, $G_{\beta\gamma}$, and $G_{\alpha,i}$, can be modeled quantitatively. We note that although these mechanisms have been modeled by several researchers to study G-protein signaling (48–51), they have not been included in most models for calcium signaling. Although the model by Lemon et al. (12) does include these details, the authors assumed a constant ligand concentration, which is appropriate only for saturating concentrations.

Mechanisms

Fig. 1 *A* shows an overall schematic of ligand-induced release of calcium from endoplasmic reticulum (ER) into cytosol, binding of calcium (Ca_i) to proteins (Pr) in the cytosol (shown) and in the ER (not shown), and other calcium-exchange fluxes to/from the ER, the extracellular space, and mitochondria. In the basal state, the channel flux from the ER, $J_{ch}$is very small and the leakage flux from the ER, $J_{ER,leak}$, is nearly balanced by the Ca^{2+} uptake back into the ER by SERCA pump, J_{SERCA}. Similarly, in the basal state, net flux across the mitochondria and the PM is also individually zero. Thus, the influx to mitochondria, $J_{mit,in}$, is balanced by the efflux from the mitochondria, $J_{mit,out}$. The Ca^{2+} outflux from cytosol to the extracellular matrix (ECM) is mediated by the PMCA (J_{PMCA}) and the Na^+/Ca^{2+} exchanger (J_{NCX}). The influx across the plasma membrane consists of a nonspecific leakage flux, $J_{PM,leak}$, and a specific flux that combines many fluxes, including the entry through store-operated channels in response to ER depletion and other effects. Following the approach of Hofer et al. (20), in this work, this specific flux, J_{PM,IP_3dep}, has been assumed to be dependent on $[IP_3]$. Ca^{2+} binds to buffer proteins in all the three compartments, the cytosol, the ER, and the mitochondria. The assumption of rapid buffering kinetics suggested by Wagner and Keizer (52) and later used by Lemon et al. (12) has been utilized in this model as well. More details, including the expressions for the fluxes, are presented in the next section (mathematical representation). Fig. 1 *B* shows the modules and reactions (both simple and lumped) that have been modeled explicitly. It can be noted that since the only measurement available to control the size of the model is $[Ca^{2+}]$ not all isoforms of different proteins are included in the model. For example, only a generic form of the protein PLCβ is included. Further, the use of lumped reactions helps reduce the number of state variables by avoiding explicit modeling of some intermediate complexes.

A text-based prototype reaction interpreter has been developed that can read both simple and complex reactions. The simple reactions have law of mass action rate expression, whereas lumped reactions follow Michaelis-Menten (M-M) kinetics or Hill dynamics. More complex formats include modulation (law of mass action, M-M, or Hill dependence). Some examples of the reactions are presented in Table S1 (Supplementary Material). Lumped-reaction formats are quite useful for model simplification.

Various modules involved in ligand-induced release of calcium from ER are discussed below. In short, binding of the ligand (C5a, denoted by L) to its receptor (C5aR, denoted by R) leads to the activation of the receptor, which in turn leads to the activation of G-protein G_i. Free $G_{\beta\gamma}$ binds with PLCβ and activates it, resulting in increased hydrolysis of PIP_2 into IP_3. Increase in the IP_3 level results in increased release of calcium from the ER.

Receptor module. Reactions 1–11 (Fig. 1 *B*, *box 1*) are as follows. Reaction 1 is activation of the receptor due to ligand binding. Reaction 2 represents binding of GRK to $G_{\beta\gamma}$ and is very fast. Reactions 3 (catalyzed by GRK) and 4 (catalyzed by GRK.$G_{\beta\gamma}$) represent desensitization of the ligand-bound active receptor (L.R), due to its phosphorylation. The activity of GRK is enhanced by the PKC.DAG.Ca_i complex due to increased phosphorylation, resulting in a negative feedback on [L.R] (53,54). This effect on the rate of reaction 3 is modeled as an enzymatic activation by calcium to avoid explicit modeling of the complexes. Reaction 5 is the dissociation of ligand and phosphorylated receptor (12,49,50). Reactions 6 and 7 are for internalization of the ligand-bound phosphorylated receptor, L.Rp (55). Reaction 7 is catalyzed by Arrestin. Reactions 8–10 together constitute receptor recovery. Reaction 8 is the dissociation of the internalized ligand-bound phosphorylated receptor, L.Ri, into the free ligand and the phosphorylated receptor (internalized form), $R_{p,i}$ (56). The internalized free ligand gets ubiquitinated and degraded. $R_{p,i}$ then gets dephosphorylated and recycled back to the surface through reaction 9 (12,48). A small part of $R_{p,i}$ also can get degraded (reaction 10). Reaction 11 is fresh receptor generation (48,51). To the best of our knowledge, in most existing models, GRK and arrestin (Arr) have not been explicitly included in calcium signaling studies, probably because knockdown data on these proteins have not been quantitatively analyzed with respect to kinetic modeling. The rate constant for reaction 4 is much higher (~100-fold) than for reaction 3, so that most phosphorylation occurs due to GRK.$G_{\beta\gamma}$ when ligand is present and due to GRK during the basal state. Similarly, internalization (reactions 6 and 7) is enhanced substantially by arrestin (buffered). Reactions 3, 4, and 7 are lumped-enzymatic reactions, as described below:

$$\text{Reaction 3: } [\text{GRK; Ca}_i]\ \text{L.R} \rightarrow \text{L.Rp (GRK and Ca}_i \text{ are enzymes)}$$

$$\text{Reaction 4: } [\text{GRK.G}_{\beta\gamma}]\ \text{L.R} \rightarrow \text{L.Rp (GRK.G}_{\beta\gamma} \text{ is an enzyme)}$$

$$\text{Reaction 7: } [\text{Arr}]\ \text{L.Rp} \rightarrow \text{L.Ri (Arr is an enzyme)}$$

GTPase cycle module. Reactions 12–16 (Fig. 1 *B*, *box 2*) depict GTPase cycle. Reactions 12 and 13 take place in the absence of active receptor and

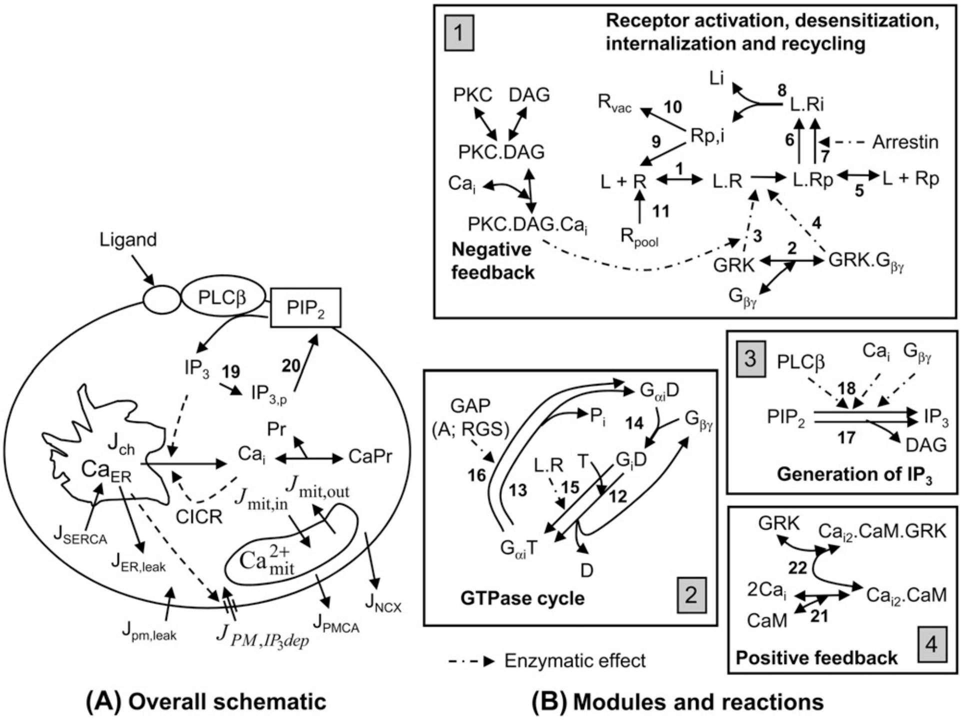

FIGURE 1 A simplified model for calcium signaling including calcium influx, ER, and mitochondrial exchange and storage, used in the conceptual-model-based computation. (*A*) Overall schematic model. The ligand C5a binds to its receptor C5aR on the plasma membrane, activating G-protein G_i. The free subunit $G_{\beta\gamma}$ binds to and activates PLCβ, which hydrolyzes PIP_2 into IP_3 and DAG. IP_3 binds to its receptor on the ER membrane and the IP_3R channels open to release calcium into the cytosol. Other calcium fluxes (e.g., with mitochondria and extracellular space) are also shown. (*B*) The mechanisms for the receptor module (*box 1*), the GTPase cycle module (*box 2*), and IP_3-generation module (*box 3*), and the feedback effects (*boxes 1 and 4*). PIP_2, phosphatidylinositol 4,5-bisphosphate; IP_3, inositol 1,4,5-trisphosphate; IP_3R, IP_3 receptor; $IP_{3,p}$, a lumped product of IP_3 phosphorylation; Ca_i, cytosolic Ca^{2+}; ER, endoplasmic reticulum; CICR, calcium-induced calcium release; SERCA, sarco(endo) plasmic reticulum calcium ATPase; PMCA, plasma membrane calcium ATPase; NCX, Na^+/Ca^{2+} exchanger; mit (subscript), mitochondria; L, ligand C5a; R, receptor C5aR; GRK, G-protein-coupled receptor kinase; CaM, calmodulin; PLCβ, phospholipase C-β; GAP, GTPase activating protein; RGS, regulator of G-protein signaling; DAG, diacylglycerol; PKC, protein kinase C; P_i, phosphate.

GTPase activating protein (GAP), respectively. Reaction 15 is similar to reaction 12 but is catalyzed by L.R, and reaction 16 is similar to reaction 13 but is catalyzed by GAP (A, RGS) (57). A more detailed description of the GTPase cycle, similar to the three-cube model in Fig. 1 *A* of Bornheimer et al. (58) but with simplification of reactions GD↔G↔GT into GD↔GT (Fig. 1 *B*, reaction *12*) and explicit modeling of $G_{\beta\gamma}$ and $G_{\alpha,i}$, was included in a detailed model, but its fit to one set of basic experimental data (stimulation with 250 nM C5a) was similar to the compact model of Fig. 1 *B*. Hence, to reduce computational complexity, only the simpler model (Fig. 1 *B*) is used for further analysis with knockdown data. Additional discussion on this simplification is presented in Supplementary Material (Approximations and the lumped/simplified mechanisms in the model). Reactions 15 and 16 are lumped-enzymatic reactions, where T is GTP, D is GDP, and A is the GAP RGS.

$$\text{Reaction 15: } [\text{L.R}]\ \text{G}_\text{i}\text{D} + \text{T} \rightarrow \text{G}_{\alpha,\text{i}}\text{T} + \text{G}_{\beta\gamma} + \text{D}$$
$$(\text{L.R is an enzyme})$$
$$\text{Reaction 16: } [\text{A}]\ \text{G}_{\alpha,\text{i}}\text{T} \rightarrow \text{G}_{\alpha,\text{i}}\text{D} + \text{P}_\text{i}\ (\text{A is an enzyme})$$

IP_3 module. In the basal state, most of the IP_3 is generated due to slow hydrolysis of PIP_2 (reaction 17), since free $G_{\beta\gamma}$ is present in very small amounts. Upon G-protein activation, dissociated $G_{\beta\gamma}$ binds to PLCβ. Cytosolic Ca^{2+} (Fig. 1 *B*, *box 3*, Ca_i) can bind to both PLCβ and PLCβ.$G_{\beta\gamma}$. Binding affinities for $G_{\beta\gamma}$ and calcium-bound forms of PLCβ are ~10 times higher than that of free PLCβ (13). Each of PLCβ.$G_{\beta\gamma}$, PLCβ.Ca_i and PLCβ.$G_{\beta\gamma}$.Ca_i catalyze hydrolysis of PIP_2, but PLCβ.$G_{\beta\gamma}$.Ca_i is the most potent. In our model, for simplification, a lumped-enzymatic reaction is used to model the enhancement due to PLCβ.$G_{\beta\gamma}$.Ca_i (see reaction 18 (Fig. 1 *B*, *box 3*)):

$$\text{Reaction 18: } [\text{Ca}_\text{i};\ \text{G}_{\beta\gamma};\ \text{PLC}\beta]\ \text{PIP}_2 \rightarrow \text{IP}_3 + \text{DAG}$$
$$(\text{enzyme is a ternary complex of Ca}_\text{i},\ \text{G}_{\beta\gamma},\ \text{and PLC}\beta).$$

As explained in Supplementary Material (Approximations and the lumped/simplified mechanisms in the model), the rate expression of the above reaction is a close approximation to an expression derived based on the assumption that all the four reversible reactions related to PLCβ are in equilibrium. Further, it is assumed that the enzymatic effect of PLCβ.$G_{\beta\gamma}$ and PLCβ.Ca_i is captured through suitable increase in the value of the rate constant. The amount of $G_{\beta\gamma}$ bound to PLCβ complexes (estimated to be ~10% of free $G_{\beta\gamma}$) is ignored for $G_{\beta\gamma}$ balance (Supplementary Material, Details of explicitly modeled reactions) in the reduced model; if all other species are included, then little reduction is achieved, and therefore it would be appropriate to model all reactions explicitly. Since PLCβ is not used in any other reaction in our model, PLCβ denotes the total PLCβ (buffered).

Reactions 19 and 20 (Fig. 1 *A*) are simplified and highly lumped representations of IP_3 metabolism, i.e., degradation/conversion to/from other inositol phosphates and back to PIP_2, with only one intermediate pseudospecies, namely, $IP_{3,p}$ or IP_3 product (12). Since oscillation is not observed in the experimental data on C5a stimulation of RAW cells, this simple representation is considered sufficient. As Mishra and Bhalla (13) have noted, such a simple description may be insufficient to model oscillatory response, even though Marhl et al. (59) have shown that interactions with the mitochondria (included in our model) can result in oscillations, especially above cytosolic $[Ca^{2+}]$ of ~0.5 μM.

It should be noted here that the free $G_{\beta\gamma}$ subunit is responsible for the activation of PLCβ, as opposed to activation by the free α subunit of a G-protein, e.g., $G_{\alpha q}T$ (G-protein G_q) upon activation of P_2Y_2 receptors, as presented by Lemon et al. (12). For the G-protein G_i, the α subunit, i.e., $G_{\alpha i}T$, does not bind to PLCβ. $G_{\beta\gamma}$ also has been implicated in calcium oscillations during fertilization (60).

Feedback effects from calmodulin. Calmodulin binds with intracellular Ca^{2+} (Ca_i) (Fig. 1 *B*, *box 4*, reaction *21*), and the resulting complex binds with GRK (reaction 22), reducing the effective amount of free GRK that can bind $G_{\beta\gamma}$. The result is reduced phosphorylation of the active receptor, and thus, this constitutes a functional positive feedback.

Mathematical representation of the model

The state variables are described by a set of ordinary differential equations (61) involving the Ca^{2+} fluxes between different cellular compartments and other fluxes due to reactions. The state variables used to model the details of ligand-induced generation of IP_3 are [L], [R], [L.R], [$G_{\beta\gamma}$], [GRK], [L.Rp], [Rp], [L.Ri], [$R_{p,i}$], [R_{pool}], [$G_{\alpha,i}T$], [$G_{\alpha,i}D$], [PIP_2], [IP_3], and [CaM] (15 of them). Calcium dynamics introduces four more state variables, $[Ca^{2+}]_i$, $[Ca^{2+}]_{ER}$, *h*, and $[Ca^{2+}]_{mit}$. $[Ca^{2+}]_{ER}$ and $[Ca^{2+}]_{mit}$ denote the concentration of free Ca^{2+} in the ER and mitochondria, respectively; *h* is explained later. Thus, the model has 19 state variables. The quantities of all chemical species are in terms of their concentrations, normalized with respect to a unit volume of the cytosol. Since, during optimization, most unknowns, e.g., parameters and initial conditions, are specified in terms of a range rather than unique values, whenever needed, a cytosolic volume of 10 pL (picoliter) or cell diameter 27 μm, typical for large macrophages, has been used.

The reaction fluxes, the related parameters, and the differential equations for the 15 state variables related to the reactions are given in Supplementary Material, Details of explicitly modeled reactions. Moieties (conservation relations) have been used to reduce the number of state variables by computing the concentrations of some species. The expressions for the other four state variables and fluxes, related to the dynamics of calcium, are given below.

Equations for calcium dynamics

$$\begin{aligned} d[Ca^{2+}]_i/dt &= \beta_i(J_{ch} + J_{ER,leak} + J_{PM,IP_3dep} - J_{SERCA} - (J_{PMCA} + J_{NCX} - J_{PM,leak}) + (J_{mit,out} - J_{mit,in}) - 2v_{21}) \\ d[Ca^{2+}]_{ER}/dt &= (\beta_{ER}/\rho_{ER})(J_{SERCA} - J_{ch} - J_{ER,leak}) \\ dh/dt &= k_{on}(Q - ([Ca^{2+}]_i + Q)h) \\ d[Ca^{2+}]_{mit}/dt &= (\beta_m/\rho_m)(J_{mit,in} - J_{mit,out}). \end{aligned} \tag{1}$$

β_i, β_{ER}, and β_m are the ratio of free calcium to total (free and bound) calcium in the cytosol, ER, and mitochondria, respectively, assuming fast buffering (equilibrium) with calcium-binding proteins. A fixed value of β_m is used. ρ_{ER} is the ratio of the ER volume to the volume of the cytosol and ρ_m is the ratio of the volume of the mitochondria to that of the cytosol. The expressions for β_i and β_{ER} are

$$\beta_i = \left(1 + \frac{Pr_{tot,e} \times K_{m,e}}{(K_{m,e} + [Ca^{2+}]_i)^2} + \frac{Pr_{tot,x} \times K_{m,x}}{(K_{m,x} + [Ca^{2+}]_i)^2}\right)^{-1},$$

$$\text{and} \quad \beta_{ER} = \left(1 + \frac{Pr_{tot,ER} \times K_{m,ER}}{(K_{m,ER} + [Ca^{2+}]_{ER})^2}\right)^{-1}, \tag{2}$$

where $Pr_{tot,e}$ is the total concentration of endogenous buffer (Ca^{2+}-binding proteins) in cytosol, $K_{m,e}$ is the dissociation constant for binding of Ca^{2+} to endogenous buffer in the cytosol, $Pr_{tot,x}$ and $K_{m,x}$ are the corresponding quantities for binding of Ca^{2+} to the exogenous/mobile buffer (fura-2) in cytosol, $Pr_{tot,ER}$ is the total buffer in the ER, and $K_{m,ER}$ is the dissociation constant for binding of Ca^{2+} to the buffer in the ER.

THE FLUX OF CALCIUM FROM ER TO CYTOSOL THROUGH THE IP_3R CHANNEL. De Young and Keizer (62) have developed a detailed model for activation/deactivation of IP_3R channels that captures the CICR effect and the biphasic behavior of the channel opening at low and extremely high calcium concentrations. Li and Rinzel (63) simplified the De Young and Keizer model (62) using time-scale analysis, which was also used by Fink et al. (35) to simulate spatial variations in neuroblastoma cells. The channel flux is given by

$$\begin{aligned} J_{ch} &= v_{max,ch} \times P_{open} \times ([Ca^{2+}]_{ER} - [Ca^{2+}]_i) \\ P_{open} &= \left(\left(\frac{[IP_3]}{[IP_3] + K_{IP3}}\right)\left(\frac{[Ca^{2+}]_i}{[Ca^{2+}]_i + K_{act}}\right)h\right)^3, \end{aligned} \tag{3}$$

where P_{open} is the IP_3R channel instantaneous open fraction or probability and *h* is the fraction of IP_3R to which calcium is not bound to the inhibitory site. K_{IP3} is the dissociation constant for binding of IP_3 on the IP_3R channel. K_{act} is the dissociation constant of Ca^{2+} binding to the activation site of the IP_3R channel. In the above expression, the second term arises due to the binding of calcium to the activation site on the IP_3R. Thus, at low calcium concentration, calcium has an activation effect on J_{ch}. However, at higher levels of calcium, the equilibrium value of *h* decreases with increasing $[Ca^{2+}]_i$ (see the differential equation for *h*). This is due to binding of calcium to the low-affinity inhibitory site on the IP_3R channel and results in biphasic response of J_{ch} with respect to $[Ca^{2+}]_i$.

FLUX THROUGH THE SERCA PUMP BACK TO ER

$$J_{SERCA} = V_{max}[Ca^{2+}]_i^2/([Ca^{2+}]_i^2 + K_P^2), \tag{4}$$

where V_{max} is the maximal rate of SERCA pump uptake and K_P is the dissociation constant of Ca^{2+} binding to the SERCA pump (12,34,35,64, 65).

LEAKAGE FLUX FROM THE ER

$$J_{ER,leak} = k_{ER,leak}([Ca^{2+}]_{ER} - [Ca^{2+}]_i), \tag{5}$$

where $k_{ER,leak}$ (s^{-1}) is the rate constant of Ca^{2+} leak flux through the ER membrane (12,59).

IP_3-DEPENDENT FLUX ACROSS THE PLASMA MEMBRANE FROM THE ECM INTO THE CYTOSOL. This is a combined effect of flux through various channels, including the SOC, which open in response to the depletion of calcium in the ER (20). Overall, this flux acts as a positive feedback mechanism to maintain cytosolic and ER calcium levels in anticipation of the emptying of the ER and the calcium efflux to the ECM (18–20,66,67). Since J_{PM,IP_3dep} includes the SOC flux, a separate SOC flux is not used.

$$J_{PM,IP_3dep} = V_{max,PM,IP_3dep}[IP_3]^2/(K^2_{m,PM,IP_3dep} + [IP_3]^2) \tag{6}$$

Leakage flux from the ECM to cytosol (20)

$$J_{\mathrm{PM,leak}} = v_{\mathrm{PM,leak}}.$$

Calcium efflux from cytosol to ECM through the PMCA and NCX

$$J_{\mathrm{PMCA}} = \frac{V_{\mathrm{max,PMCA,l}}[\mathrm{Ca}^{2+}]_{\mathrm{i}}^{2}}{[\mathrm{Ca}^{2+}]_{\mathrm{i}}^{2} + K_{\mathrm{m,PMCA,l}}^{2}} + \frac{V_{\mathrm{max,PMCA,h}}[\mathrm{Ca}^{2+}]_{\mathrm{i}}^{5}}{[\mathrm{Ca}^{2+}]_{\mathrm{i}}^{5} + K_{\mathrm{m,PMCA,h}}^{5}} \quad \text{and}$$

$$J_{\mathrm{NCX}} = \frac{V_{\mathrm{max,NCX}}[\mathrm{Ca}^{2+}]_{\mathrm{i}}}{[\mathrm{Ca}^{2+}]_{\mathrm{i}} + K_{\mathrm{m,NCX}}}. \qquad (7)$$

$J_{\mathrm{PMCA}}$is due to two pumps, a low-capacity (high-affinity) and a high-capacity (low-affinity) pump (34). $V_{\mathrm{max,PMCA,l}}$ and $V_{\mathrm{max,PMCA,h}}$ are the maximum capacities of the low and high capacity PMCA pump, respectively, and $K_{\mathrm{m,PMCA,l}}$ and $K_{\mathrm{m,PMCA,h}}$ are the Ca^{2+} concentrations for half-maximal flux through the two pumps. Similarly, $V_{\mathrm{max,NCX}}$ is the maximum flux through the $\mathrm{Na}^{+}/\mathrm{Ca}^{2+}$ exchanger and $K_{\mathrm{m,NCX}}$ is the corresponding Michaelis-Menten constant for the binding of Ca^{2+}.

Calcium uptake into and efflux from mitochondria. Based on the model of Marhl et al. (59), calcium flux into mitochondria (68) is given by

$$J_{\mathrm{mit,in}} = k_{\mathrm{in}}[\mathrm{Ca}^{2+}]_{\mathrm{i}}^{4}/(K_{2}^{4} + [\mathrm{Ca}^{2+}]_{\mathrm{i}}^{4}), \qquad (8)$$

where k_{in} is the maximum permeability for uptake of Ca^{2+} by the mitochondrial uniporter and K_2 is the half-maximal $[\mathrm{Ca}^{2+}]_{\mathrm{i}}$. Marhl et al. (59) have used a Hill coefficient of 8, since this uptake rate is quite steep with respect to increased concentration of the cytosolic Ca^{2+}. However, we have used a much smaller value of 4 (still quite steep) to be able to fit experimental data. The efflux term is given by

$$J_{\mathrm{mit,out}} = (k_{\mathrm{out}}[\mathrm{Ca}^{2+}]_{\mathrm{i}}^{2}/(K_{3}^{2} + [\mathrm{Ca}^{2+}]_{\mathrm{i}}^{2}) + k_{\mathrm{m}})[\mathrm{Ca}^{2+}]_{\mathrm{mit}}, \qquad (9)$$

where k_{out} is the maximal rate for the $\mathrm{Na}^{+}/\mathrm{Ca}^{2+}$ exchanger and permeability transition pores (PTPs), K_3 is the corresponding half-maximal $[\mathrm{Ca}^{2+}]_{\mathrm{i}}$ for efflux and k_{m} is the rate constant for a nonspecific leak flux.

In the expression for *dh*/*dt* (Eq. 1), Q is an effective Michaelis constant capturing the $\mathrm{IP_3R}$ channel's calcium-dependent inhibition, and is given by (63)

$$Q = K_{\mathrm{inh}}([\mathrm{IP_3}] + K_{\mathrm{IP3}})/([\mathrm{IP_3}] + d_3), \qquad (10)$$

where K_{inh} is the dissociation constant for Ca^{2+} binding to the inhibition site and d_3 is the dissociation constant of $\mathrm{IP_3}$ binding when the Ca^{2+} inhibitory site is occupied. Finally, $v_{21}$is the rate of reaction 21, the binding of two Ca^{2+} to calmodulin (Fig. 1 *B*, *box 4*). The values of the parameters used in the above expressions are listed in Table S2 (Supplementary Material). Initial conditions for the state variables and the values of other parameters, such as the concentrations of buffered species/enzymes, are listed in Supplementary Material, Conservation parameters, buffered species and the initial conditions.

Solution of the ordinary differential equations, and parameter estimation. The procedures for solving the ordinary differential equations and parameter estimation using a hybrid stochastic-search-based algorithm that combines genetic algorithm (GA), differential evolution (DE), and particle-swarm optimization (PSO) are summarized in Supplementary Material. The objective function and the constraints used for parameter estimation are also given in Supplementary Material.

Prediction of dose response. We predicted the dose response of C5a using the best set of parameter values for the master dataset. The C5a dose is varied from 1 nM to 500 nM. Between different runs, the only change is in the ligand strength i.e., [C5a] at $t = t_{\mathrm{LA}}$ (time of ligand addition). To perform the simulation, the system is solved to get the initial basal state (phase 1), and then the system evolves at the basal conditions till $t = t_{\mathrm{LA}}$ (phase 2, part 1). At $t = t_{\mathrm{LA}}$, [C5a] is reset to the dose strength, e.g., 30 nM, corresponding to the experimental dataset 1. All other initial conditions remain at the basal steady-state level, and simulation is carried out (phase 2, part 2).

Sensitivity analysis. To consider both small and large changes, each parameter (one at a time) is perturbed by multiplying its base value by factors [⅛, ¼, ½, 1, 2, 4, 8]. After simulation, the shift in the basal level (baseline shift), the peak-height compared to the respective basal level, and their sum, i.e., the peak height from the basal level for the base set, are computed. Since our fit-error function included both the good fit to basal level and good fit to response after ligand addition, a weighted average of normalized baseline shift B (weight 0.5), and normalized variation in peak height (H) is used to rank the parameters. B is computed as the maximum absolute baseline shift divided by the maximum peak height across the seven perturbations. H is computed as the maximum absolute difference in peak height across the seven perturbations divided by the maximum peak height. Let b_{i} be the baseline shift and h_{i} be the peak height for the perturbations. Then, mathematically,

$$B = \max(abs(b_{\mathrm{i}}))/\max(h_{\mathrm{i}}) \text{ and}$$
$$H = (\max(h_{\mathrm{i}}) - \min(h_{\mathrm{i}}))/\max(h_{\mathrm{i}}),$$

where h_{i} is always nonnegative. The parameters are sorted in the decreasing order of ($0.5 \times B + H$), i.e., from the most to least sensitive. It should be noted that only the response of $[\mathrm{Ca}^{2+}]_{\mathrm{i}}$ is considered here for sensitivity.

Variation between different subpopulations of cells

For a chosen strength of the ligand C5a, when the experiments were repeated with multiple subpopulations of cells, though the qualitative response was similar, substantial quantitative variation is observed in key features such as basal level, peak height, etc. This variation is present across different control datasets, as well as in the basal levels of knockdown cell lines. This variability is an inevitable fact concerning biological systems (69). It cannot be explained by using a single set of values of the kinetic parameters and the initial conditions, since concentrations and fluxes vary across subpopulations. As mentioned earlier, if the basal levels were similar across different subpopulations (datasets) without knockdown, a common set of parameter values could have been used. However, in the data used, variation in the basal level even without knockdown is as much as 30% of the peak height in some datasets, e.g., compare datasets 1 and 2 (Fig. 2, *panel 5*, and Fig. 3, *panel 2*, in Results).

To utilize multiple datasets corresponding to different subpopulations of cells without imposing unrealistic constraints, some of the parameters should be allowed to vary. These parameters can be of the following types: 1), initial condition of state variables ([R], $[\mathrm{G}_{\beta\gamma}]$, and $[\mathrm{G}_{\alpha,\mathrm{i}}\mathrm{D}]$); 2), unknown variable concentration of a buffered species ($\mathrm{PLC}\beta_{\mathrm{tot}}$, [A], and [Arr]); 3), a lumped parameter, specified externally or related to a lumped reaction, in which all enzymes or modulators are not specified explicitly ($[\mathrm{X}_{\mathrm{PIP2\_gen}}]$); and 4), parameters related to the capacity and shape of cell (ρ_{ER},$\mathrm{Pr}_{\mathrm{tot,e}}$, $\mathrm{Pr}_{\mathrm{tot,x}}$, $\mathrm{Pr}_{\mathrm{tot,ER}}$, $v_{\mathrm{max,ch}}$, V_{max}, $V_{\mathrm{max,PMCA,l}}$, $V_{\mathrm{max,PMCA,h}}$, and $V_{\mathrm{max,PM,IP_3dep}}$). Initial conditions of $[\mathrm{PIP_2}]$, [GRK] and [CaM] are allowed to vary across subpopulations by allowing $\mathrm{PIP}_{2,\mathrm{tot}}$, $\mathrm{GRK}_{\mathrm{tot}}$, and $\mathrm{CaM}_{\mathrm{tot}}$ to vary, respectively. Other parameters, such as those related to basic reactions are maintained constant across datasets.

This flexibility requires the generation of simulation/optimization code that is dependent on the specification of the data. This is the only effective approach to utilize such data for kinetic modeling. Thus, a total of 19 parameters are allowed to vary from one subpopulation to another. Several other combinations of fewer parameters were found to be unsatisfactory. The parameters are separated into two classes, nonvarying and varying. Corresponding to the chosen datasets, first the master list of parameters is related to one basic dataset (referred to as ''Master dataset''). Here, the first dataset (the control data on RGS10 knockdown) is chosen as the master dataset (Supplementary Material, Table S3). The total number of parameters to be estimated that are associated with the master dataset is 65. This includes $k_{\mathrm{f},9}$, which was optimized between 7.0×10^{-4} and 0.001 but later set to 0.001 to get nearly full recovery of the receptor in 30–35 min. Of these 65 parameters, 46 are common to all subpopulations, whereas the 19 varying parameters are instantiated for each dataset. Essentially, for each additional dataset, the list of varying parameters is appended to the list. The list of varying parameters is tracked so that during simulation stage, appropriate parameter assignment

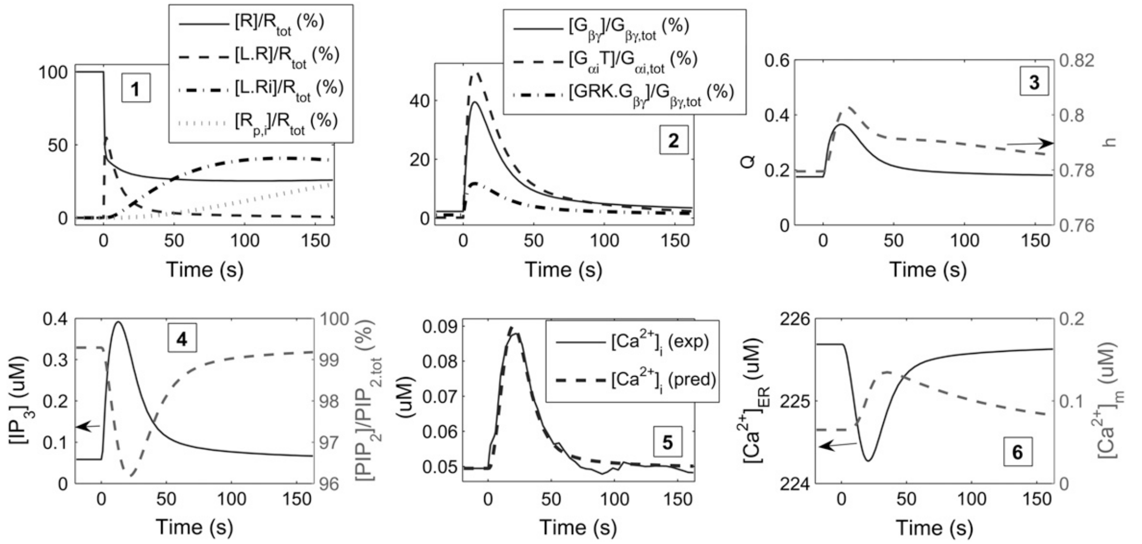

FIGURE 2 Time course of several state variables including [Ca^{2+}]$_i$ for dataset 1 (control for knockdown of RGS with 30 nM C5a), as predicted by using the best parameter values. (*1*) Fraction (percentage as compared to total surface receptors, R$_{tot}$) of free surface receptors ([R], *solid line*), ligand-bound active receptors ([L.R], *dashed line*), internalized ligand-bound phosphorylated receptors ([L.Ri], *dash-dotted line*), and internalized free receptors ([R$_{p,i}$], *dotted line*). Substantial change (decrease in [R] and increase in [L.R]) is observed soon after ligand addition ($t_{LA} = 0$ s). Upon phosphorylation, the active receptor, L.R, gets internalized. Thus, [L.R*i*] starts to increase after a few seconds and reaches its peak at ~120 s. As L.Ri dissociates into the ligand and R$_{p,i}$, [R$_{p,i}$] shows an increase after a delay of ~20 s. (*2*) Percentage of G$_{\beta\gamma}$ in the free state (*solid line*) and bound to GRK (*dash-dotted line*), and percentage of active G-protein ([G$_{\alpha,i}$T], *dashed line*). All three lag behind [L.R] and exhibit qualitatively similar profiles. (*3*) Indicators of IP$_3$-receptor channel activity: *Q*, the effective Michaelis constant (*solid line*), and *h* (*dashed line*). As indicated by the arrow, the *y* axes for *Q* and *h* are on the left- and right-hand sides, respectively. (*4*) Concentration of IP$_3$ (*solid line*, the left *y* axis) and the fraction of unhydrolyzed PIP$_2$ (*dashed line*, the right *y* axis). (*5*) Fit of the model prediction (*dashed line*) to experimental data (*solid line*). (*6*) Time course of [Ca^{2+}]$_{ER}$ (the left *y* axis) and [Ca^{2+}]$_{mit}$ (labeled as [Ca^{2+}]$_m$ on the right *y* axis).

can be made for each dataset. The list of varying parameters cannot include a calculated parameter. Any calculated parameters are recalculated to maintain the constraints on the parameters.

With four datasets, the total number of unknown parameters becomes $46 + 4 \times 19 = 122$, an increase by a factor of ~2. The total amount of experimental data has increased by a factor of 4. Hence, at least in principle, this scheme results in more constraints on the parameter space. In reality, the result could be somewhat different, because with nonlinear dependence on the parameters, even a small increase in the dimensionality of the search space could result in substantial effective freedom in the search space. Since the constraints described in Supplementary Material are applied to all datasets, this problem gets alleviated to some extent.

There is one potential problem in letting the variable parameters vary for different subpopulations across the entire range used for optimization. In reality, the values of a variable parameter across different subpopulations are within a certain factor of each other. For example, $V_{max,PMCA,l}$ is optimized between 0.01 and 0.5. Its value for different subpopulations could be in the range 0.05–0.12, within a factor of 2.4 of each other. Thus, constraints must be imposed on how much such parameters could differ from each other across different populations. We generate the values of such parameters (p_i) for the master dataset and then require that the corresponding values for other datasets (populations), p_i^k (for the k^{th} dataset), should be within a factor range of 0.5–1.5 (user-defined) as compared to p_i, ensuring that such parameters cannot deviate by more than a factor of 3 (= 1.5/0.5) between any two datasets. Thus, the additional parameters for other datasets are not the actual values of the parameters (p_i^k), but instead are the corresponding ratios (r_i^k). Using the ratio r_i^k, p_i^k is easily computed as $p_i^k = p_i \times r_i^k$. The resulting value is clipped at the lower or upper bound on the parameter value and is then ready for use in simulation. The calculated parameters are recomputed for each dataset with these corresponding values of the other parameters. A major advantage of this approach of handling the variability is that the additional ratio parameters to be estimated are all in a small range of (0.5–1.5) instead of being dependent on the optimization range of the actual parameter itself. This approach provides an elegant way of relating the variable parameters (intrinsic biochemical properties) of a knockdown dataset and the corresponding control dataset.

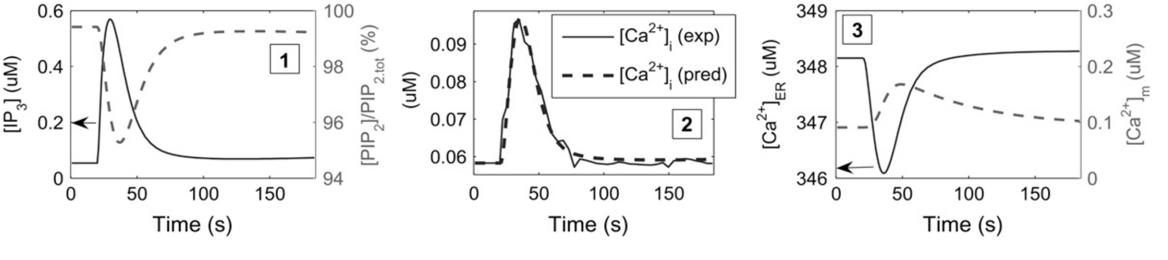

FIGURE 3 Time course of state variables for dataset 2 (control for knockdown of G$_{\alpha i}$ with 100 nM C5a). (*1*) [IP$_3$] (*solid line*, left *y* axis) and the fraction of unhydrolyzed PIP$_2$ (*dashed line*, right *y* axis). (*2*) Fit of the model prediction (*dashed line*) to the experimental data (*solid line*). (*3*) Time course of [Ca^{2+}]$_{ER}$ (*solid line*, left *y* axis) and [Ca^{2+}]$_{mit}$ (*dashed*, right *y* axis).

Modeling of knockdown data

In the shRNAi-based knockdown cell lines, cells reach a new initial basal state (AfCS protocol PP00000211 (23)). This new basal state is a manifestation of the knockdown of the protein of interest. Hence, to model the knockdown mathematically, once the values of the variable parameters are assigned through the approach described in the previous section, the knockdowns are emulated. Any calculated parameters that could be dependent on the value of the variable being altered due to knockdown are computed only then, and the initial basal steady state is computed. The value with knockdown is computed as $x_{\mathrm{KD}} = x \times (1 - \%\ knockdown/100)$, where x is the base value of the affected variable (initial condition, concentration of a buffered protein, etc.) that would have been effective in the absence of knockdown, x_{KD} is the value with knockdown, and *%knockdown* is the level of knockdown expressed in percentage.

It should be noted that for the ratio constraint on $\mathrm{G}_{\beta\gamma,\mathrm{tot}}/\mathrm{G}_{\alpha,\mathrm{i,tot}}$ (Supplementary Material, The objective function and the constraints), the values before knockdown are used. After the knockdown, this ratio constraint need not be satisfied, especially with the knockdown of $\mathrm{G}_{\beta\gamma}$ or $\mathrm{G}_{\alpha,\mathrm{i}}$ ($\mathrm{G}_{\alpha,\mathrm{i}}2$ and $\mathrm{G}_{\alpha,\mathrm{i}}3$). Further, the G-proteins from other families such as $\mathrm{G}_{\alpha,\mathrm{q}}$ are not modeled. It is assumed that the total amount of all G-proteins in the cell is around five times that of $\mathrm{G}_{\alpha,\mathrm{i}}$. Since the experimental data on the knockdown of $\mathrm{G}_{\alpha,\mathrm{i}}$ is based upon the actual cell, with no effect on other G-proteins, for modeling purposes, the effective knockdown level is reduced by a factor of 5. Without this scaling, absurd values of the parameters and response were obtained.

Modeling and prediction of knockdown response requires computation of a new basal state for nontraining scenarios before simulating the model with stimulus as described in Supplementary Material, Computation of new basal state for knockdown scenarios.

RESULTS

Constrained parameter values and fit to experimental data

The detailed results of parameter estimation using the hybrid genetic algorithm-differential evolution-particle swarm optimization approach are presented in Supplementary Material. The essential results are presented here briefly. The best parameter values of the common parameters and the base values of the variable parameters are listed in Table 1. Table S6 (Supplementary Material) lists two other such parameter-value sets that fit the experimental data nearly to the same degree as the best set and satisfy all constraints. Some parameters, such as $K_{\mathrm{m,x}}$, $\mathrm{Pr}_{\mathrm{tot,ER}}$, $K_{\mathrm{m,NCX}}$, and k_{m}vary by a factor of 1.5 or more across the three sets (Table S6), suggesting some redundancy and nonlinear relationships among the parameters.

Validation of the rapid-buffering assumption

Measurement of $[\mathrm{Ca}^{2+}]_{\mathrm{i}}$ through fluorescence using fura-2 as well as Eq. 2 are based on the assumption that binding and dissociation of $[\mathrm{Ca}^{2+}]_{\mathrm{i}}$ with the endogenous and exogenous/mobile buffers is very rapid as compared to the timescale of measurements (~4 s; interpolated at 1 s). The fact that the association and dissociation rate constants are rarely specified in the literature (46,47), suggests that these assumptions are universally taken for granted. For the exogenous buffer fura-2, a K_{D} of 0.2–0.24 μM ($K_{\mathrm{m,x}}$ in Table S2) is reported (12,13,35). For endogenous buffer, $K_{\mathrm{m,e}} \approx 10\,\mu\mathrm{M}$ for cytosolic proteins and $K_{\mathrm{m,ER}} \approx 1000\,\mu\mathrm{M}$ for ER proteins is used. Mishra and Bhalla (13) use a dissociation rate constant (k_{b}) of 1 s^{-1} whenever unknown. At steady state, the net rate of these reactions is zero. To test whether these reactions quickly reach dynamic equilibrium when Ca^{2+} levels change, dynamic simulation of these reactions is carried out for two different values of k_{b}, viz. $k_{\mathrm{b}} = 0.1$ and 1 s^{-1}. $K_{\mathrm{m,x}}$ and $K_{\mathrm{m,e}}$ are chosen as in Table 1. During the transients, the ratio of the rate of the reverse reaction to the forward reactions varies between 0.68 and 1.28 for $k_{\mathrm{b}} = 0.1\ \mathrm{s}^{-1}$ and between 0.95 and 1.02 for $k_{\mathrm{b}} = 1.0\ \mathrm{s}^{-1}$. Thus, for $k_{\mathrm{b}} = 1.0\ \mathrm{s}^{-1}$, the equilibrium assumption is valid.

TABLE 1 The best parameter values for dataset 1

Parameter name (unit)	Value	Parameter name	Value
$\mathrm{Pr}_{\mathrm{tot,e}}$ (μM)	1.91 *E* + 02	$K_{\mathrm{m,Ca_{i2}.CaM}}$	8.36 *E* − 01
$K_{\mathrm{m,e}}$ (μM)	2.43 *E* + 00	$V_{\mathrm{max,PM,IP_3dep}}$	2.26 *E* − 01
$\mathrm{Pr}_{\mathrm{tot,x}}$ (μM)	8.77 *E* + 00	$k_{\mathrm{f,1}}$	5.89 *E* + 01
$K_{\mathrm{m,x}}$ (μM)	1.39 *E* − 01	$k_{\mathrm{b,1}}$	2.02 *E* − 01
$\mathrm{Pr}_{\mathrm{tot,ER}}$ (μM)	6.02 *E* + 04	$k_{\mathrm{b,2}}$	2.52 *E* + 01
$K_{\mathrm{m,ER}}$ (μM)	5.46 *E* + 02	$k_{\mathrm{f,3}}$	1.22 *E* − 01
ρ_{ER}	5.33 *E* − 02	$K_{\mathrm{m,Ca_i,3}}$	1.01 *E* − 01
k_{on} (μM/s)	1.04 *E* − 01	$k_{\mathrm{f,4}}$	1.26*E + 02*
K_{inh} (μM)	1.00 *E* + 00	$k_{\mathrm{f,5}}$	2.05 *E* − 03
$v_{\mathrm{max,ch}}$ (s^{-1})	1.89 *E* − 01	$k_{\mathrm{f,6}}$	6.62 *E* − 04
K_{IP3} (μM)	1.36 *E* − 01	$k_{\mathrm{f,7}}$	1.67 *E* + 00
d_3 (μM)	1.05 *E* + 00	$k_{\mathrm{f,8}}$	5.00 *E* − 03
K_{act} (μM)	8.14 *E* − 02	$k_{\mathrm{f,12}}$	3.67 *E* − 07
V_{max} (μM/s)	1.14 *E* + 02	$k_{\mathrm{f,13}}$	5.00 *E* − 02
K_{P} (μM)	7.54 *E* − 01	$k_{\mathrm{f,14}}$	1.59 *E* + 04
$k_{\mathrm{ER,leak}}$ (s^{-1})	2.03 *E* − 003	$k_{\mathrm{b,14}}$	4.18 *E* − 02
$V_{\mathrm{max,PMCA,l}}$ (μM/s)	8.93 *E* − 02	$k_{\mathrm{f,15}}$	1.38 *E* − 003
$K_{\mathrm{m,PMCA,l}}$ (μM)	1.13 *E* − 01	$K_{\mathrm{m,G_iD,15}}$	6.81 *E* − 02
$V_{\mathrm{max,PMCA,h}}$ (μM/s)	5.90 *E* − 01	$k_{\mathrm{cat,16}}$	1.54 *E* + 00
$K_{\mathrm{m,PMCA,h}}$ (μM)	4.42 *E* − 01	$\mathrm{K}_{\mathrm{m,16}}$	2.35 *E* − 01
$V_{\mathrm{max,NCX}}$ (μM/s)	1.00 *E* − 01	$k_{\mathrm{f,17}}$	5.00 *E* − 04
$K_{\mathrm{m,NCX}}$ (μM)	1.00 *E* + 00	$k_{\mathrm{f,18}}$	5.07 *E* + 02
k_{in} (μM/s)	5.06 *E* + 02	$K_{\mathrm{m,Ca_i,18}}$	3.64 *E* − 01
k_{out} (s^{-1})	4.76 *E* + 02	$K_{\mathrm{m,G_{\beta\gamma},18}}$	3.64 *E* − 01
K_2 (μM)	9.92 *E* − 01	$k_{\mathrm{f,19}}$	1.49 *E* + 00
k_{m} (s^{-1})	1.50 *E* − 03	$k_{\mathrm{f,22}}$	1.10 *E* − 02
$PLC\beta_{\mathrm{tot}}$	5.61 *E* − 03	$k_{\mathrm{b,22}}$	2.75 *E* − 03
$PIP_{2,\mathrm{tot}}$	1.29 *E* + 02	$[A]$	1.02 *E* − 02
$X_{\mathrm{PIP2\_gen}}$	1.01 *E* − 01	$[Arr]$	8.63 *E* − 03
GRK_{tot}	2.59 *E* − 03	IC:$[R]$	4.11 *E* − 02
$K_{\mathrm{m,GRK}}$	5.07 *E* − 03	IC:$[G_{\beta\gamma}]$	8.28 *E* − 03
$\mathrm{CaM}_{\mathrm{tot}}$	3.98 *E* + 00	IC:$[G_{\alpha,\mathrm{i}}D]$	8.12 *E* − 03

The values given are the same as in column 2 (Set 1, best) of Table S6, and in the same order. The computed parameters are not listed here.

Constrained parameter values versus values based on legacy data

As mentioned earlier, parameter-constraining using in vivo data was necessary, since the legacy values based on in vitro data in different cell types reported in the literature could not predict experimental data even within an order of magnitude. It is possible that the difference in the values of the individual parameters based on in vitro or legacy data and in vivo data may be small, but this difference is present in many parameters whose overall effect becomes very large. Here we compare these values for some of the parameters to justify the use of in vivo data for developing computational models.

Parameters for the receptor activation/desensitization. The bounds for these parameters, listed in Table S4 (Supplementary Material), were based on Hoffman et al. (48), Pumiglia et al. (70), Woolf and Linderman (50), Chen et al. (71,72), Daaka et al. (73), and Sklar and co-workers (74,75). None of the values were measured or designed for the RAW 264.7 cell system. To cite a few examples, Hoffman et al. (48) used $k_{f,1} = 84 \pm 19$ μM/s, whereas Sklar et al. (74) used 17–27 μM/s for the N-formyl peptide receptor system. We used the bounds 10–100 μM/s. The optimized/constrained value of $k_{f,1}$ is 58.9 μM/s for the best set (Table 1). For the two other sets, it is 60 μM/s (Table S6). The bounds for $k_{b,1}$, chosen similarly, were 0.1–1 s^{-1}. Hoffman et al. (48) used $k_{b,1} = 0.37 \pm 0.1$ s^{-1} for the N-formyl peptide receptor system. The optimized value is 0.2 s^{-1} (Tables 1 and S6), well within a factor of 2, even though they are different systems. We had also used the constraint $0.001 \le k_{b,1}/k_{f,1} \le 0.02$ μM that was based upon the values suggested by Linderman and colleagues (48–50). This constraint on the K_D is also within the value suggested specifically for C5a-C5aR, viz. 1–100 nM for neutrophils and eosinophils, by Leslie (37). Thus, a fair amount of legacy information was used to ensure that the constrained parameter values satisfy the biochemistry embedded in the literature values. The list goes on for the parameters related to reactions 2–11. For brevity, we refer to Tables 1, S4, and S6 and the constraints listed in Supplementary Material.

Parameters for G-protein module (reactions 12–16). The bounds for most of the parameters of these reactions were chosen based upon the values suggested by Bornheimer et al. (58), Ross and Wilkie (76), and Biddlecome et al. (77). Since reactions 12 and 15 use the lumped scheme (Supplementary Material), the parameter values suggested in Bornheimer et al. (58), Ross and Wilkie (76), and Biddlecome et al. (77) were scaled accordingly to compute the bounds. For reaction 12 (basal activity), the bounds on $k_{f,12}$ were 1.0×10^{-7} to 3.0×10^{-6} μM/s (Table S4), whereas the optimized value is 3.67×10^{-7} for the best set (Table 1). Due to lumping, and scaling of the parameter, this value cannot be directly compared, but the values of the raw parameters were based on a large body of literature (58). For reaction 13 (intrinsic GTPase activity), the bounds on $k_{f,13}$ were 0.05–0.07 s^{-1} (Table S4), as suggested by Ross and Wilkie (76) and Sprang (78). The optimized value, 0.05 s^{-1}, actually matches exactly with the value for the G-protein $G_{\alpha,i1}$ (78,79). For RGS-catalyzed hydrolysis (reaction 16), Ross and Wilkie (76) report $k_{cat,16} = 15$–25 s^{-1} for $G_{\alpha,q}$-PLCβ and $G_{\alpha,q}$-RGS4 systems. We allowed a range of 1–50 s^{-1}, since G-protein $G_{\alpha,i}$ is from a different family (Table S4). The optimized value is 1.54 s^{-1} (Table 1). This lower value reflects the observation of Ross and Wilkie (76) that RGS has a selectivity for $G_{\alpha,q}$ over $G_{\alpha,i}$. Such corroborations increase our confidence that the parameter values are in the right range.

Parameters for the IP_3 module. Since the mechanisms proposed by Li and Rinzel (63) are directly used to model the release of Ca^{2+} from ER, the related parameters were constrained within the bounds gleaned from their work (63). The notation used by Fink et al. (35) is used here. Despite some relaxation to compensate for the simplification, the optimized values are quite close to those suggested by Li and Rinzel (63). Several examples are given here. The optimized value of k_{on}, the on-rate constant for Ca^{2+} binding to an inhibitory site, 0.104 μM/s (Table 1) is close to the value 0.2 μM/s suggested by De Young and Keizer (62) and used by Li and Rinzel (63), even though a wide bound of 0.1–4.0 was specified (Table S2), since Fink et al. (35) had used a value of 2.7 μM/s. The same is true for K_{inh}, the K_D for Ca^{2+} binding to an inhibitory site. The bounds were 1–1.5 s^{-1} (Table S2). The optimized value is 1.0 s^{-1}, whereas Li and Rinzel (63) have used 1.05 s^{-1}. Fink et al. (35) had used a much lower value of 0.2 s^{-1}, but we biased it to Li and Rinzel's value (63) by specifying a lower bound of 1. For K_{IP3} (K_M for activation of IP_3R by IP_3), Hofer et al. (20) used 0.3 μM and Li and Rinzel (63) used 0.13 μM (Table S2). We optimized in the range 0.1–1, and the optimized value of 0.136 (Table 1) agrees well with data in Li and Rinzel (63). Similar agreement is found for the parameters d_3 and K_{act} (Tables S2 and 1).

Parameters for calcium dynamics. There are ~20 parameters related to various processes such as Ca^{2+} binding to cytosolic and ER proteins, and exchange with the ER across the plasma membrane and the mitochondria. The most important parameters in regulating the calcium dynamics are related to the exchange with ER ($v_{max,ch}$, V_{max}, K_P, and $k_{ER,leak}$) and binding to the calcium-binding proteins ($Pr_{tot,e}$, $K_{m,e}$, $Pr_{tot,x}$, and $K_{m,x}$). The bounds for $v_{max,ch}$ (maximum intrinsic channel flux per μM of $[Ca^{2+}]_{ER}$) were based upon comparison of the corresponding values used by Marhl et al. (59), Lemon et al. (12), and Fink et al. (35) to get a peak flux of ~1.5 μM/s with $[Ca^{2+}]_{ER} =$ ~200–500 μM (Table S2). There is wide difference in the values used by Marhl et al. (59) (4100 s^{-1}) and Lemon et al. (12) (575 s^{-1}). Both these are very high, since the authors have used much lower $[Ca^{2+}]_{ER}$. We get an optimized value of 0.189 s^{-1}. This low value in our model is justified, since we have much higher $[Ca^{2+}]_{ER}$ and much lower $[Ca^{2+}]_i$. As an example, Fink et al. (35) use 3500 μM/s as maximum flux and peak height of the $[Ca^{2+}]_i$ time-course is as much as 1 μM. In our case, peak height is ~0.06 μM (experimental data), lower by a factor of ~17, and the equivalent maximum flux is ~30–50 μM/s, lower by a factor of ~70–100. After binding to the proteins, the remaining excess calcium is cleared primarily by the SERCA pump, which follows Hill dynamics with $\alpha = 2$. The ultrasensitivity and the saturation nature of the SERCA pump justify the need to get a 70–100 times lower maximum flux to get ~17 times lower peak height of $[Ca^{2+}]_i$. The optimized value of K_P (half-saturation level for SERCA pump), 0.754 μM, is about double the value used by Lemon et al. (12), whereas V_{max} (maximum flux through the SERCA pump), 114 μM/s, is ~2.5 times higher than that used by Lemon et al. (12). Larger V_{max} was necessary to get a flux of ~1 μM/s, since $[Ca^{2+}]_i$ is about two to four times lower. Such differences in the parameter values, as compared to values reported previously for other specific or nonspecific cell types, justify the in vivo data-based constraining of the parameters. Although using the values reported in the literature for other cell types will result in similar gross qualitative shapes (e.g., first rise and then return to basal levels), the quantitative differences can be of more than an order of magnitude as explained above. Even the finer details of qualitative shape, such as the time constants for the rise and decay phases, can differ significantly, further strengthening the case for cell-specific constraining of the parameters. The bounds for the parameters $Pr_{tot,e}$, $K_{m,e}$, $Pr_{tot,x}$, and $K_{m,x}$ were based on values used by others (12,35,52,59). The optimized value of $Pr_{tot,e}$, 191 μM, is about the same as used in Marhl et al. (59) and Lemon et al. (12) (120–150 μM). The value of $K_{m,e}$, 2.43 μM, is lower than reported in Lemon et al. (12) but much higher than 0.1 μM, the value used by Marhl et al. (59). Thus, there is huge variation in the literature values. Since Ca^{2+} binds to the endogenous buffer with a low affinity, a value >1 μM is justified. On the contrary, Ca^{2+} has high affinity for the exogenous buffer. For fura-2, $K_{m,x} = 0.2$ μM is mostly reported. In our model, we relaxed it somewhat to partially compensate for uncertainty in $Pr_{tot,e}$, $K_{m,e}$, and $Pr_{tot,x}$, but still the optimized value of 0.139 μM for the best set is not much different. In fact, it is 0.2 μM for set 2. The lower values of $K_{m,e}$ and $K_{m,x}$ could be partially due to the lower $[Ca^{2+}]_i$. Somewhat higher $Pr_{tot,e}$ could offset this, but the fact that there are several pools of proteins with somewhat different K_D values points to the approximations made here.

Variation in parameters across datasets due to sub-populational variability

Due to subpopulational variability within the best set itself, the values of the variable parameters for the different datasets are substantially different, as is evident from the values of the ratio parameters listed in Table 2. In Table 2, ratio values are listed for datasets 2–4. For dataset 1, this value is 1 by default. As mentioned earlier (Materials and Methods), for datasets 2–4, the actual value of the variable is computed by multiplying the raw ratio (r_i^k) by the value of the parameter for dataset 1 (p_i) and then limiting the resulting value to the lower or upper bound, i.e., $p_i^k = p_i \times r_i^k$; if $p_i^k < LB$, $p_i^k = LB$, and if $p_i^k > UB$, $p_i^k = UB$. Then the true value of the ratio parameter, reported in Table 2, is computed as $r_{i,TRUE}^k = p_i^k / p_i$. Of all the 19 ratio parameters, the range of variation (MAX/MIN ratio across the four datasets) is <1.5 for eight parameters. For the parameters ρ_{ER}, $v_{max,ch}$, and $V_{max,PMCA,l}$, this range is ≥2, which is not surprising since all three exert large control on calcium dynamics through the size factor, maximal flux through the IP_3R channel, and the expulsion of calcium to the extracellular space. For other parameters, the range of variation is between 1.5 and 2. Overall, these values suggest that substantial variation is exhibited by different subpopulations of cells. The specifics of how these differences help explain the observed variety of calcium response in different datasets is presented below in the context of fit to experimental data.

TABLE 2 Values of the ratio parameters for parameters that vary among datasets and the computed parameters (for best parameter-value set only)

	Ratio values			
Parameter name	Dataset 2	Dataset 3	Dataset 4	MAX/MIN
ρ_{ER}	$1.00 E + 00$	$1.26 E + 00$	$5.74 E - 01$	$2.19 E + 00$
$Pr_{tot,e}$	$1.02 E + 00$	$5.28 E - 01$	$5.68 E - 01$	$1.92 E + 00$
$Pr_{tot,x}$	$5.61 E - 01$	$8.62 E - 01$	$9.43 E - 01$	$1.78 E + 00$
$Pr_{tot,ER}$	$7.30 E - 01$	$1.12 E + 00$	$9.66 E - 01$	$1.53 E + 00$
$v_{max,ch}$	$5.30 E - 01$	$1.50 E + 00$	$1.50 E + 00$	$2.83 E + 00$
V_{max}	$1.08 E + 00$	$1.38 E + 00$	$1.04 E + 00$	$1.38 E + 00$
$PLC\beta_{tot}$	$1.31 E + 00$	$8.92 E - 01$	$1.44 E + 00$	$1.62 E + 00$
$PIP_{2,tot}$	$9.44 E - 01$	$9.44 E - 01$	$1.24 E + 00$	$1.32 E + 00$
X_{PIP2_gen}	$1.22 E + 00$	$9.89 E - 01$	$9.89 E - 01$	$1.24 E + 00$
IC:$[R]$	$9.73 E - 01$	$1.07 E + 00$	$1.23 E + 00$	$1.27 E + 00$
IC:$[G_{\beta\gamma}]$	$9.67 E - 01$	$9.67 E - 01$	$9.67 E - 01$	$1.03 E + 00$
GRK_{tot}	$1.16 E + 00$	$1.16 E + 00$	$9.65 E - 01$	$1.20 E + 00$
CaM_{tot}	$7.15 E - 01$	$5.53 E - 01$	$5.99 E - 01$	$1.81 E + 00$
IC:$[G_{\alpha,i}D]$	$9.85 E - 01$	$9.85 E - 01$	$9.85 E - 01$	$1.02 E + 00$
$[A]$	$9.42 E - 01$	$1.17 E + 00$	$1.18 E + 00$	$1.25 E + 00$
$[Arr]$	$1.39 E + 00$	$9.27 E - 01$	$9.27 E - 01$	$1.50 E + 00$
V_{max,PM,IP_3dep}	$6.62 E - 01$	$7.44 E - 01$	$1.10 E + 00$	$1.67 E + 00$
$V_{max,PMCA,l}$	$5.00 E - 01$	$5.11 E - 01$	$6.82 E - 01$	$2.00 E + 00$
$V_{max,PMCA,h}$	$8.48 E - 01$	$1.50 E + 00$	$9.53 E - 01$	$1.77 E + 00$
Parameters computed using steady-state constraints:				
$v_{PM,leak}$	$1.45 E - 02$	$1.31 E - 02$	$1.49 E - 02$	$1.40 E + 00$
IC:$[Ca^{2+}]_{ER}$	$3.48 E + 02$	$3.18 E + 02$	$2.55 E + 02$	$1.54 E + 00$
IC:$[Ca^{2+}]_{mit}$	$9.11 E - 02$	$9.22 E - 02$	$7.30 E - 02$	$1.42 E + 00$

Consistency of the model and parameters with experimental data and the relevance of subpopulational variability

Figs. 2–5 show the fit of the predicted $[Ca^{2+}]_i$ to the corresponding experimental data for the four datasets. The predicted time course for other key variables and biochemical species such as the concentrations of free surface receptors and ligand-bound active receptors, free $G_{\beta\gamma}$, h, and the concentrations of IP_3, $[Ca^{2+}]_{ER}$, etc., are also shown. Before getting into the details of the specific features of the dynamic response, it should be noted that good fit between the experimental data used for estimating the parameters and the model predictions corresponding to the best set of parameter values is obtained (Figs. 2, *panel 5*, 3, *panel 2*, 4, *panel 5*, and 5, *panel 2*). The main features of the predicted dynamic response for each dataset are discussed below.

Dataset 1 illustrates the dynamic response of various modules. Results for dataset 1 (the master dataset, the control for RGS knockdown with addition of 30 nM C5a) are shown in Fig. 2.

Activated receptor is quickly desensitized and remains internalized for a long time. Fig. 2, *panel 1* shows the dynamic response of several species from the receptor module. C5a binds to C5aR quickly, and within seconds a substantial increase in [L.R] and a sharp decrease in [R] are observed. After the first few seconds, [R] reaches a pseudo-steady-state level of 10–11 nM $\approx$ (R_{tot} – 30) (Table 1). As L.R gets phosphorylated, [L.R] starts to decrease. Some L.Rp gets internalized. Thus, [L.Ri] starts to increase and reaches its peak at ~120 s. As L.Ri dissociates into the ligand and $R_{p,i}$, [$R_{p,i}$] increases after a delay of ~20 s. Interestingly, [L.Ri] remains high for a long time, since its dissociation rate, $k_{f,8} = 0.005\ s^{-1}$, is low (Table 1). Likewise, Once [Rp,i] reaches a high level within 10 min, it remains high for even longer since the receptor recovery is even slower ($k_{f,9} = 0.001\ s^{-1}$). A more detailed analysis of the receptor recovery is presented in the companion to this article.

Negative feedback regulation of receptor activity is mediated by the activated G-protein. Fig. 2, *panel 2* shows the dynamics of G-protein. Since the activation of G-protein follows the activation of the receptor, [$G_{\beta\gamma}$], [GRK.$G_{\beta\gamma}$], and [$G_{\alpha,i}$] lag behind [L.R]. Further, they exhibit qualitatively similar profiles. The peak levels of [$G_{\beta\gamma}$] and [GRK.$G_{\beta\gamma}$] are in an ~3:1 ratio. Substantial GRK.$G_{\beta\gamma}$ results in quick desensitization of the activated receptor.

Large variation in Q and a relatively smaller variation in h is observed. Fig. 2, *panel 3* displays the time course of Q, the effective Michaelis constant (*solid lines*), and h (*dashed lines*). Q varies between 0.2 and 0.4, whereas variation in h is much smaller. The peak of Q precedes the peak of h by 5–10 seconds, and both rise and decay of h is slower than that of Q. Q closely follows [IP_3] (Fig. 2, *panels 3* and *4*) because $sign(dQ/dt) = sign(d[IP_3]/dt)$ with $K_{IP3} < d_3$ (62).

Peak IP_3 levels are more than five times higher than the basal level. Fig. 2, *panel 4* shows [IP_3] and the fraction of unhydrolyzed PIP_2. The maximal [IP_3] (~0.4 μM) is 6–7 times higher than the basal level. Only <4% of PIP_2 is hydrolyzed and most of that is present as the phosphorylation product of IP_3, $IP_{3,p}$. The actual values of the fraction of open IP_3R channels are different from their equilibrium values (not shown); *dh*/*dt* is justified (Eq. 1). However, this departure from equilibrium is small compared to that observed in oscillatory scenarios (63).

The model and the parameters are consistent with data. Fig. 2, *panel 5* shows the excellent fit of the model prediction to experimental data. The peaks are quite close both in terms of magnitude and the occurrence time. The rise and decay phases are also captured well.

Mitochondrial uptake is slower compared to the ER uptake. Fig. 2, *panel 6* shows the time course of $[Ca^{2+}]_{ER}$ and $[Ca^{2+}]_{mit}$ (labeled $[Ca^{2+}]_m$). As $[Ca^{2+}]_i$ starts to increase, $[Ca^{2+}]_{ER}$ starts to decrease, since Ca^{2+} comes out of ER. As $[Ca^{2+}]_i$ increases, $[Ca^{2+}]_{mit}$ also increases. Even though the dynamics of $J_{mit,out}$ has a Hill dynamics dependence on $[Ca^{2+}]_i$, due to a large value of K_3, $J_{mit,out}$ is small and, hence, decay of $[Ca^{2+}]_{mit}$ starts after a longer time.

Dataset 2 provides computational evidence of subpopulational variability in several components. The results for dataset 2 (the control dataset for knockdown of $G_{\alpha i}$ with addition of 100 nM C5a at $t_{LA} = 20$ s) are shown in Fig. 3. The qualitative features of the quantities shown in panels 1–3 of Fig. 2 for dataset 1 are quite similar to those for dataset 2. Hence these are not shown again for dataset 2. One exception is the response of [R], which is similar to its response for dataset 3 (Fig. 4, *panel 1*). This is because in both datasets 2 and 3, the ligand strength is 100 nM. Here, we discuss the response of [IP_3] and [PIP_2] (Fig. 3, *panel 1*), fit of predicted $[Ca^{2+}]_i$ to the experimental data (Fig. 3, *panel 2*) and the response of $[Ca^{2+}]_{ER}$ and $[Ca^{2+}]_{mit}$ (Fig. 3, *panel 3*).

Higher PLCβ pool results in higher peak [IP_3]. As shown in panel 1, the peak [IP_3] level for dataset 2 is higher compared to dataset 1. This can be attributed to higher C5a (100 nM) and a higher level of PLCβ_{tot} (ratio factor 1.31, Table 2), other factors such as R_{tot}, $G_{\beta\gamma}$, and $PIP_{2,tot}$ being similar (Table 2). Higher PLCβ_{tot} is sufficient to result in higher levels of [IP_3]. As will be discussed later, the half-maximal effect concentration (EC_{50}) for dose response of C5a, the dose required to reach half-maximal response, is ~18 nM, well below 30 nM. Hence, 100 nM C5a would not cause a substantial increase in the peak [IP_3] levels compared to 30 nM C5a. Thus, the higher level of [IP_3] is mainly attributed to higher PLCβ_{tot}. In fact, the ratio 1.31 correlates well with the ratio of the peak levels of [IP_3] for datasets 1 and 2 (Figs. 2, *panel 4* and 3, *panel 1*).

Subpopulational variability explains anomalous peak calcium response. Fig. 3, *panel 2* shows the excellent fit of the predicted data to the experimental data. It can be noted that even though the basal levels of $[Ca^{2+}]_i$ and several other species such as [IP_3] and [PIP_2] are different between datasets 1 and 2, the height of the peaks of $[Ca^{2+}]_i$ are quite similar. The ratio of the peak values of $[Ca^{2+}]_i$ is 0.097/0.086 = 1.13. At first this appears paradoxical, due to a higher peak level of [IP_3]. However, this anomaly can be resolved by observing the subpopulational variability. In particular, $v_{max,ch}$, the maximal flux through the IP_3R channels, is only half as compared to its value for dataset 1 (ratio 0.53, Table 2). Other differences in the values of the parameters for datasets 1 and 2 that help explain this anomaly are described in Supplementary Material, Similar peak-heights of $[Ca^{2+}]_i$ for datasets 1 and 2.

Larger basal $[Ca^{2+}]_i$ requires larger $[Ca^{2+}]_{ER}$ and leads to larger $[Ca^{2+}]_{MIT}$. Fig. 3, *panel 3* shows that $[Ca^{2+}]_{ER}$ and $[Ca^{2+}]_{mit}$ are both higher during the basal steady state, as well as during the transients compared to dataset 1. This is reasonable, since basal $[Ca^{2+}]_i$ is also higher for dataset 2. Further, since V_{max} is higher, a higher level of $[Ca^{2+}]_{ER}$ is required to maintain the sought basal state. A lower value of $v_{max,ch}$ also contributes to this, albeit to a lesser degree.

Dataset 3 sheds light on the altered state upon the knockdown of $G_{\alpha i}$. The results for dataset 3 (85% knockdown of $G_{\alpha i}$, with addition of 100 nM C5a at $t_{LA} = 20$ s) are shown in Fig. 4. The layout of the figure is similar to that of Fig. 2 for dataset 1.

High-dose results in depletion of the surface receptors. Since the ligand concentration, 100 nM, is higher than $R_{tot} = 41$ nM, shortly after ligand addition, [R] drops to almost 0 (Fig. 4, *panel 1*). After the first few seconds [L.R] also drops quickly and most of the receptor is present as L.Ri and $R_{p,i}$. The dynamics of the receptor module for dataset 2 is similar.

Knockdown of $G_{\alpha i}$ results in higher basal and peak levels of $[G_{\beta\gamma}]$ and $[IP_3]$. Fig. 4, *panel 2* shows the response of the GTPase cycle module. Even though the qualitative shapes of the time-evolution plots are similar to those seen in panel 2 of Fig. 2, there are two major quantitative differences. The first is that the basal levels of $[G_{\beta\gamma}]$ and $[GRK.G_{\beta\gamma}]$ are well above zero, because due to the knockdown of $G_{\alpha i}$ there is not enough $G_{\alpha i}D$ to bind with $G_{\beta\gamma}$, and hence, some $G_{\beta\gamma}$ is present in the free active state. $[GRK.G_{\beta\gamma}]$ follows a similar trend. The second difference is that the peak activity of the G-protein is relatively higher. The direct consequence of the higher levels of $[G_{\beta\gamma}]$ is higher basal and peak levels of $[IP_3]$ and Q, and both follow a common trend, as discussed for dataset 1 (Fig. 4, *panels 3* and *4*).

The response of Q and h are qualitatively opposite. The dynamic response of h is very different compared to other datasets (Fig. 4, *panel 3*). After an initial increase in h with $[IP_3]$ and Q, h quickly reaches its equilibrium value (with respect to $[IP_3]$ or Q) and then starts to decrease even though Q is still rising. The reason is that $[Ca^{2+}]_i$ and h reach high enough levels to make dh/dt negative. Clearly, the biphasic behavior of the channel opening is the result of an increase in $[IP_3]$ and $[Ca^{2+}]_i$ and a decrease in h. Higher depletion of PIP_2 is observed (Fig. 4, *panel 4*).

Knockdown of $G\alpha i$ results in partial depletion of the ER. The fit to experimental data in this case is good (Fig. 4, *panel 5*). Basal levels are similar to those for dataset 2. However, since the basal level of $[IP_3]$ and, hence, the open fraction of IP_3R channels, is higher for dataset 3 compared to dataset 2, to achieve similar $[Ca^{2+}]_i$, a lower basal $[Ca^{2+}]_{ER}$ is required (Fig. 4, *panel 6*). The large slope of $[Ca^{2+}]_i$ during the rise phase also required a higher value of $v_{max,ch}$ (Table 2). With these accumulating increasing effects, to satisfy the desired peak response and slope of the decay phase, a higher V_{max} is required (Table 2).

At higher $[Ca^{2+}]_i$, response is hastened due to ultrasensitivity. Basal $[Ca^{2+}]_{mit}$ is similar to that for dataset 2 but higher than for dataset 1 (Fig. 4, *panel 6*). However, peak $[Ca^{2+}]_{mit}$ is much higher compared to any other dataset, due to the ultrasensitive dependence of $J_{mit,in}$ on $[Ca^{2+}]_i$. With increased $[Ca^{2+}]_{mit}$, the decay phase is also steeper compared to other datasets (Fig. 4, *panel 6*). Another distinction deserving mention is that as the response returns toward the basal level, in datasets 1 and 3, $[Ca^{2+}]_{ER}$ approaches from a lower level (i.e., it does not cross the basal level), whereas for dataset 2, it approaches the basal state from above the basal level (after $t \approx 120$ s). This could have been the onset point for oscillation if high levels of $[IP_3]$ could have been sustained for a longer time leading to somewhat higher $[Ca^{2+}]_i$.

Dataset 4 also validates the necessity of subpopulational variability. The results for dataset 4 (83% knockdown of $PLC\beta$, with addition of 100 nM C5a at $t_{LA} = 20$ s) are shown in Fig. 5. The three panels are similar to the panels in Fig. 3 for dataset 2.

Subpopulational variability is required. In Fig. 5, *panel 1*, it is clear that due to reduced $PLC\beta$, lower $[IP_3]$ is obtained. In fact, $PLC\beta_{tot}$ without knockdown is actually higher than for dataset 1, viz. the ratio $PLC\beta_{tot,set\ 4}/PLC\beta_{tot,set\ 1} = 1.44$ (optimized value); otherwise, even lower peak $[IP_3]$ would have been observed. As much as 98.5% of PIP_2 remains unhydrolyzed.

Oscillations are not possible. The plots in Fig. 5, *panel 2* suggest a good fit to experimental data during the rise and the initial decay. However, during the later phase, the fit is not good. We discard the possibility of oscillations here and conclude that there is some sort of systematic error in the measurement itself; oscillations can occur only if $[Ca^{2+}]_i$ drops much below its basal levels due to very high activity of the SERCA pump while maintaining high $[IP_3]$. None of this is observed since $[IP_3]$ levels are well below 0.2 μM (Fig. 5, *panel 1*) and $[Ca^{2+}]_i$ approaches the basal level from above the basal level (Fig. 5, *panel 2*). Given that the basal level of $[Ca^{2+}]_i$ is between the corresponding values for datasets 1 and 3, a similar trend for basal $[Ca^{2+}]_{ER}$ is reasonable (Fig. 5, *panel 3*).

Prediction of dose response

Dose response of a ligand is one of the most useful and experimentally measurable indicators of the ligand efficacy for a target. We predicted the dose response as outlined in Materials and Methods. The main results are described below.

Full response results from 75 nM C5a, and with increasing dose, the rise time decreases. The simulation results are presented in Fig. 6. Fig. 6 *A* shows the temporal response of $[Ca^{2+}]_i$ for increasing doses of C5a. The doses shown are for C5a = [1 2 3 5 10 20 30 50 75 100 250 500] nM. Response for all state variables is near saturation for C5a = 50 nM, and it is difficult to distinguish between the curves for C5a ≥ 75 nM. The temporal response curve for 30 nM C5a for which experimental data is available is labeled to show that ~80% saturation is achieved at this level. The time to reach peak decreases as the C5a dose is increased. This is because of the partial switchlike ultrasensitive behavior of J_{SERCA} with respect to $[Ca^{2+}]_i$. More precisely, at lower doses, due to low J_{ch}, to reach sufficient $[Ca^{2+}]_i$ and J_{SERCA}, longer time is needed. Though not very visible in the plot, near the peaks, the curve for C5a = 50 nM is slightly to the right compared

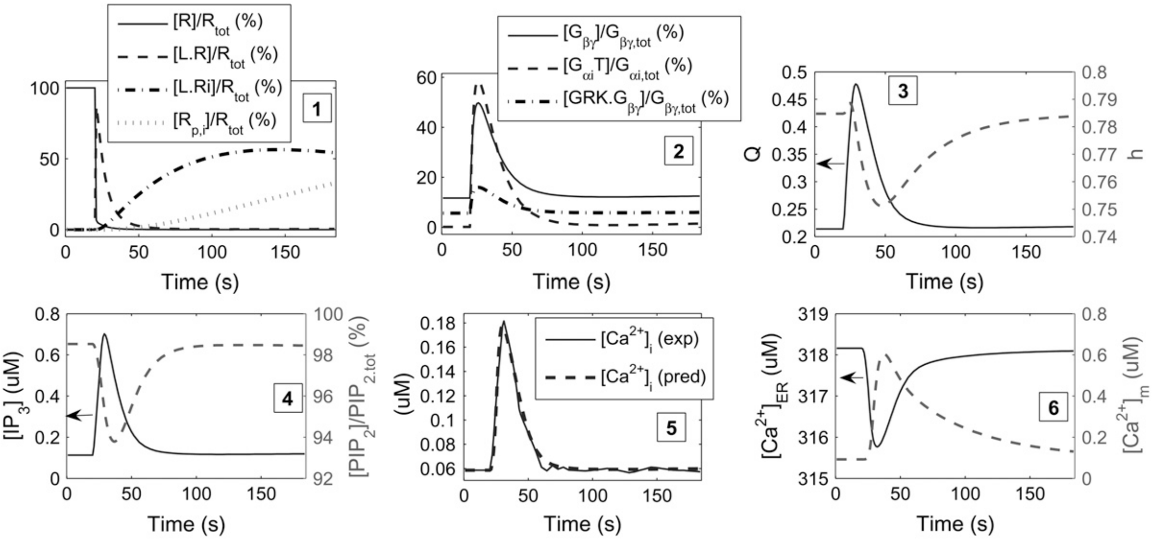

FIGURE 4 Time course of state variables for dataset 3 (85% knockdown of $G_{\alpha i}$ with 100 nM C5a). (*1*) Fraction of [R] (*solid line*), [L.R] (*dashed line*), [L.Ri] (*dash-dotted line*), and [$R_{p,i}$] (*dotted line*). (*2*) Percentage of [$G_{\beta\gamma}$] (*solid line*) and [GRK.$G_{\beta\gamma}$] (*dash-dotted line*), and percentage of [$G_{\alpha,i}$T*]* (*dashed line*). (*3*) *Q* (*solid line*, left *y* axis), and *h* (*dashed line*, right *y* axis). (*4*) [IP_3] (*solid line*, left *y* axis) and the fraction of PIP_2 (*dashed line*, right *y* axis). (*5*) Fit of the model prediction (*dashed line*) to experimental data (*solid line*). (*6*) Time course of [Ca^{2+}]$_{ER}$ (*solid line*, left *y* axis) and [Ca^{2+}]$_{mit}$ (*dashed line*, right *y* axis).

to the curves for higher doses. Also, the curve for C5a = 30 nM crosses the curves for higher doses at $t \geq 30$ s. It is difficult to suggest that this crisscross behavior could be related to the EC_{50} value for the ligand.

HIGHER DOSES RESULT IN BIMODAL RESPONSE OF THE ACTIVATED RECEPTORS. Fig. 6 *B* shows the fraction (percentage) of the total receptors that are bound to the ligand and active ($R_{tot} = 0.041$ μM for each simulation). Since receptor activation is the first step in the cascade after ligand binding, the active fraction increases rapidly and then starts to decrease as the active receptor gets phosphorylated. The maximal fraction of active receptors is close to 100% suggesting that for C5a ≥ 100 nM, receptors are indeed saturated. As shown later, since L and R bind in a 1:1 ratio, the EC_{50} level for C5a is about half of R_{tot}. After about $t = 100$ s, some of the receptors are recycled back. For lower doses, all the ligand is used up by this time, and hence, [L.R] does not show an increase after this time. However, for C5a ≥ 50 nM, since some unused ligand remains in the system, as soon as some receptor is recycled, an increase in [L.R] is observed (not visible). Receptor recycling will be discussed in greater detail in the companion to this article.

THE TOTAL SURFACE RECEPTOR, AND NOT THE TOTAL $G_{\beta\gamma}$, IS THE LIMITING FACTOR FOR THE MAXIMAL RESPONSE. Fig. 6 *C* shows the fraction of free active [$G_{\beta\gamma}$]. The trend is similar to that for the active receptor shown in Fig. 6 *B* but with a slight delay and a larger effective time constant, because the GTPase cycle module is the second stage in the cascade. Similar to [L.R], with C5a ≥ 50 nM, a secondary increase in [$G_{\beta\gamma}$] is observed after $t > 100$ s. Even with almost all the receptor active, maximal free [$G_{\beta\gamma}$] is only 40%. Also, due to the basal activity of the GTPase cycle, ~2.3% of total [$G_{\beta\gamma}$] is free in the absence of the ligand. Had the total number of surface receptors been larger, larger maximal [$G_{\beta\gamma}$] could have been observed. Thus, the total amount of receptors seems to be the bottleneck for obtaining a higher response. In fact, it is easy to see that there are saturation or maximal capacity effect at various stages of the signaling cascade. For example, if R_{tot} were not the bottleneck, then the next bottleneck would be $G_{\beta\gamma,tot}$, as [$G_{\beta\gamma}$] is limited by $G_{\beta\gamma,tot}$. It is this capacity limit that results

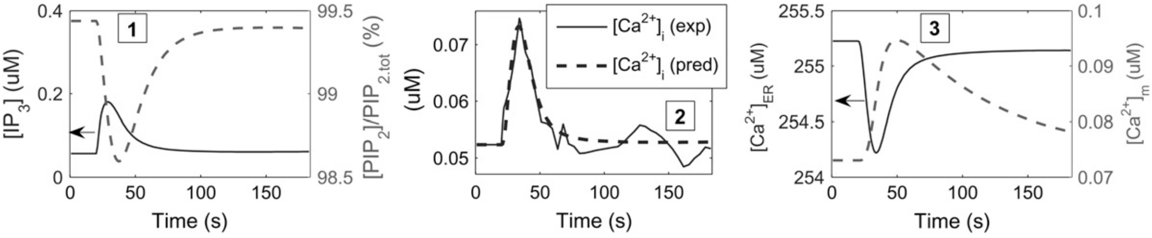

FIGURE 5 Time course of state variables for dataset 4 (83% knockdown of PLCβ with 100 nM C5a). (*1*) [IP_3] (*solid line*, left *y* axis) and the fraction of PIP_2 (*dashed line*, right *y* axis). (*2*) Fit of the model prediction (*dashed line*) to experimental data (*solid line*). (*3*) Time course of [Ca^{2+}]$_{ER}$ (*solid line*, left *y* axis) and [Ca^{2+}]$_{mit}$ (*dashed line*, right *y* axis).

in M-M or Hill dynamics (ultrasensitivity) effect in signaling modules.

Dose response shows ultrasensitivity and the EC$_{50}$ value is about half the total surface receptors. Fig. 6 *D* shows the dynamic response of [IP$_3$], which is nearly identical to that of [G$_{\beta\gamma}$] qualitatively. The dynamic response of [Ca^{2+}]$_{ER}$ shown in Fig. 6 *E* is qualitatively similar to that of [G$_{\beta\gamma}$] and [IP$_3$] except that [Ca^{2+}]$_{ER}$ decreases as the ligand is applied. Fig. 6 *F* shows the dose-response curve. The sigmoidal shape on the semilog plot indicates the ultrasensitivity effect. The EC$_{50}$ value of C5a is18 nM and the effective Hill coefficient is ~2. As mentioned earlier, the EC$_{50}$ value is about half of R$_{tot}$. In fact, the value of 18 nM is based on the intersection of the dose-response curve with the half-maximal horizontal line on the semilog plot. On a linear-scale plot, this value turns out to be ~20 nM, which is even closer to half of R$_{tot}$. Indeed, the maximal response is limited by R$_{tot}$. Starting from the ligand to the cytosolic Ca^{2+}, there are several mechanisms that exhibit M-M kinetics or ultrasensitivity. The receptor module, the GTPase module and the PLCβ module exhibit M-M kinetics for the relevant fluxes, whereas J_{ch} shows ultrasensitivity with a coefficient of 3 with respect to the preceding events, e.g., activation level of the IP$_3$R. Hence one might expect a hill coefficient (α) of 5 or even more for the dose-response curve. However, in practice, $\alpha > 2$ is rarely observed. This is because one of the stages/modules serves as the limiting module, e.g., R$_{tot}$ in this case. Hence, effectively, $1 < \alpha < 2$ is observed. In fact, on a linear scale, the dose-response curve appears to exhibit M-M behavior. The ultrasensitivity of the expression for J_{SERCA} also counterbalances the ultrasensitivity of the activation steps. Finally, the qualitative shape of the dose-response curve is similar to those obtained by Mishra and Bhalla (13) for glutamate stimulus (Fig. 5 in (13)).

The EC$_{50}$ value of 18–20 nM is comparable to those observed in the AfCS data (5–20 nM). As mentioned earlier, substantial variation is observed between the control experiments for different knockdowns. As an example, the peak height for the control for knockdown of G$_\beta$-2 is ~70 nM for 100 nM C5a (ID ECD031202B (29)), whereas for control of knockdown of C5aR the peak height is ~45 nM for 10 nM C5a (ID ECD031118B) and ~50 nM for 100 nM C5a (ID ECD031118B), suggesting that EC$_{50}$ could be even below 5 nM, depending on R$_{tot}$.

Multiparametric variability analysis

Given the nonlinearity of the system, to comprehensively assess the effect of changes in the parameters and the important initial states, using the results of optimization, a multiparametric variability analysis (MPVA) is carried out (58,80). In this approach, the parameter values obtained during the stochastic-search-based optimization that fit the data well are analyzed. The parameters are sorted according to their

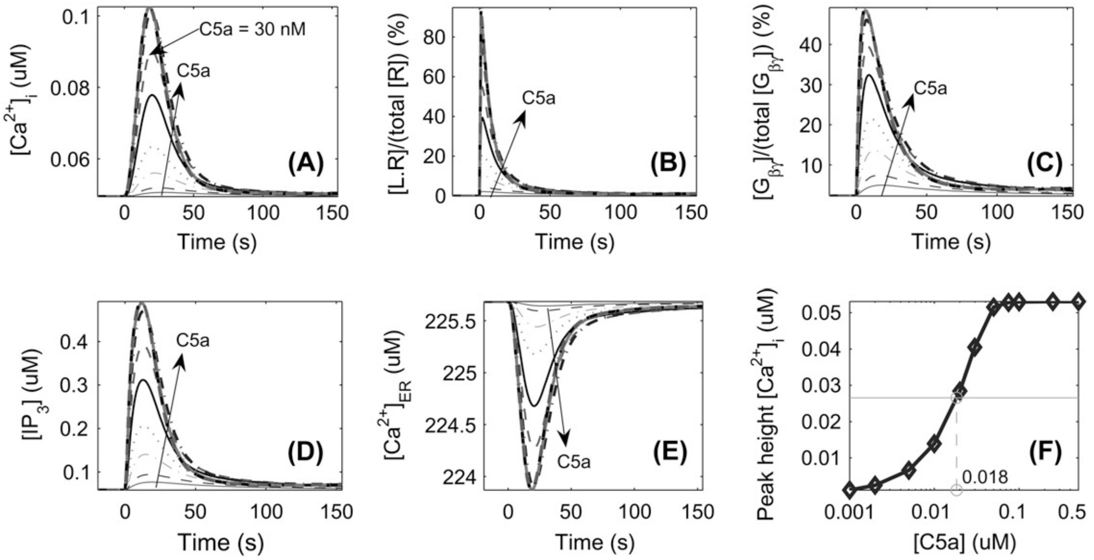

FIGURE 6 Prediction of dose response of C5a using the parameters for the master dataset. As the C5a dose is varied from 1 nM to 500 nM, the system is simulated each time and dynamic responses of [Ca^{2+}]$_i$ and several other state variables is recorded. (A) Temporal response of [Ca^{2+}]$_i$ for increasing doses of C5a. The response for C5a = 30 nM, for which experimental data is available, is labeled. The time to reach peak decreases as the C5a dose is increased. (*B*) Fraction (percentage) of the receptor in ligand-bound active form (R$_{tot}$ = 0.041 μM for each simulation). Since receptor activation is the first step in the cascade after ligand binding, the active fraction increases rapidly and then starts to decrease as the active receptor gets phosphorylated. (*C*) Fraction of free-active [G$_{\beta\gamma}$]. The trend is similar to that for the active receptor but with a slight delay and a larger effective time constant. Even with almost all the receptor active, maximal free [G$_{\beta\gamma}$] is only 40%. Also, due to the basal activity of the GTPase cycle, ~2.3% of total [G$_{\beta\gamma}$] is free in the absence of the ligand. (*D*) Dynamic response of [IP$_3$]. (*E*) Dynamic response of [Ca^{2+}]$_{ER}$. (*F*) Dose response curve: The sigmoidal shape on the semilog plot indicates the ultrasensitivity effect. The half-maximal effect concentration (EC$_{50}$) of C5a is 18 nM and the effective Hill coefficient is ~2.

decreasing range (ratio of the maximum to minimum value, MAX/MIN) across this good set of parameter values. The system is less sensitive to the parameters with larger MAX/MIN or range (80). On the contrary, the system is more sensitive to the parameters with a narrow range (80). Table S7 (Supplementary Material) lists the important statistics about the parameters and then lists the parameters in the order of increasing MAX/MIN, i.e., from most to least important. The four most constrained parameters are IC:[$G_{\beta\gamma}$], IC:[$G_{\alpha,i}$D], $k_{f,18}$, and GRK_{tot}, in that order (IC stands for initial condition). This makes sense, because any imbalance in $G_{\beta\gamma,tot}$ or $G_{\alpha i,tot}$ leads to large changes, as observed in dataset 3. $k_{f,18}$ directly affects the production of IP_3, and hence it is a crucial parameter. Similarly, GRK_{tot} is important since GRK competes against $G_{\alpha,i}$D for binding to $G_{\beta\gamma}$. Using the values of the parameters across the good sets, a pseudoprobability distribution is computed for each parameter. The probability distribution, plotted in Fig. S2 and discussed in Supplementary Material, shows that good diversity was maintained during optimization.

Since the MAX and MIN values can potentially depend on the lower bound and upper bound used in optimization and on the cutoff fit-error used to define the good sets, the regular parametric sensitivity analysis is also carried out.

Parametric-sensitivity analysis

First, the sensitivity of temporal calcium response, peak height, and basal level to changes in individual parameters is studied. Then sensitivity of dose response is studied. Finally, global change in the parameters is studied. Whenever appropriate, results are compared with those obtained by Mishra and Bhalla (13).

Sensitivity analysis of temporal response

As described in Materials and Methods, a weighted criterion, $0.5B + H$ (where B is the normalized baseline-shift and H is the normalized variation in the peak height), is used to rank the parameters according to sensitivity. The resulting list is shown in S8 (Supplementary Material). Table S8 lists only those parameters for which $B \geq 0.05$ or $H \geq 0.5$ to indicate a sufficiently large change in the response for parametric deviation ranging over a factor of 64. The most sensitive parameters according to sensitivity analysis are IC:[$G_{\beta\gamma}$], IC:[$G_{\alpha,i}$D], $k_{ER,leak}$ and K_P (dissociation constant for SERCA pump). For these parameters, the temporal response and baseline-shift, peak height, and their sum are shown in Fig. 7. Baseline-shift and/or peak height are very large for each of these parameters. Both $k_{ER,leak}$ and K_P exert strong control on the basal level, since during the basal state the leakage flux from the ER to the cytosol is balanced mainly by the SERCA pump flux back to the ER. Though the baseline shift and the sum of baseline shift and peak height are monotonic as the parameter is increased, the same is not true about the peak height itself. Peak height shows highly nonlinear behavior for changes in IC:[$G_{\beta\gamma}$] and IC:[$G_{\alpha,i}$D]. They are not even monotonic. The peak heights decrease for an increase as well as a decrease in the value of these two parameters. Peak height is nonmonotonic for $k_{ER,leak}$, whereas it is monotonic for K_P. The nonmonotonic nature is due to excessive baseline shift.

Most of the parameters listed in column 3 are related to the production of IP_3 or the binding of IP_3 to the IP_3R channel. This is in agreement with the legacy knowledge about the crucial role of ER and IP_3 dynamics in regulating the cytosolic calcium (62,63,81–87). Mishra and Bhalla (13) report similar results on the central role of IP_3 dynamics. It should be noted that here, only $[Ca^{2+}]_i$ response is included for sensitivity analysis. If the response of some other components, such as [IP_3], [L.R], etc., also were included in the sensitivity analysis, the ranking would potentially change. Comparison of the sorted lists of parameters in Tables S7 and S8 shows that despite some differences, the group of the first 15–20 most sensitive parameters is the same in both tables. For example, IC:[$G_{\beta\gamma}$] and IC:[$G_{\alpha,i}$D] are at the top in both lists. $k_{f,18}$, GRK_{tot} (Table S7, near the top) are within the first 18 most sensitive parameters in Table S8. Similarly, $k_{ER,leak}$ and K_P(Table S8, near the top) are the 15th and 12th most sensitive parameters in Table S7. Thus, MPVA and parametric sensitivity analysis provide complementary views.

Perturbation of IC:[$G_{\alpha,i}$D] is especially interesting because our results show that at reduced IC:[$G_{\alpha,i}$D], the relative peak height is decreased, since the basal level is increased substantially (Fig. 7, *top row*, *two rightmost panels*). This is in agreement with the pattern observed in the AfCS data on knockdown of IC:[$G_{\alpha,i}$D] (29). Thus, our model can explain both an increase and a decrease in peak height for the knockdown of $G_{\alpha,i}$.

These results for the remaining 32 parameters listed in Table S8 are similar (not shown). Other details are listed in Table S8. For many parameters, the baseline shift was negligible, whereas the change in peak height was substantial. For these parameters, the peak height is monotonic with increasing value of the parameter. The peak height is nonmonotonic for parameters $k_{f,19}$, $PIP_{2,tot}$, and K_{IP3}. Most of the parameters with no baseline shift are related to the reactions. Also, for the enzymatic reactions and other M-M kinetics and Hill-dynamics-based expressions, the monotonic natures for parameters V_{max} and K_m are opposite. Some examples include reaction 18 ($k_{f,18}$ and $K_{m,G_{\beta\gamma},18}$ and $K_{m,Ca_i,18}$), parameters V_{max} and K_P (Fig. 7), and parameters $V_{max,PMCA,l}$ and $K_{m,PMCA,l}$.

Dose response under single-parameter variation

For a chosen parameter, the value of the parameter is perturbed by the factors [⅛ ¼ ½ 1 2 4 8], and dose response is predicted for each case. The maximum deviation from the basal level of the base response with no perturbation is considered the peak height, $\max(\Delta[Ca^{2+}]_i)$. Since increase in the dose results in higher peaks (Fig. 5 *F*), the parameters resulting in increase in overall peak height (the sum), such as IC:[$G_{\beta\gamma}$], $k_{ER,leak}$, and K_P in Fig. 7, and IC:[R] (not shown),

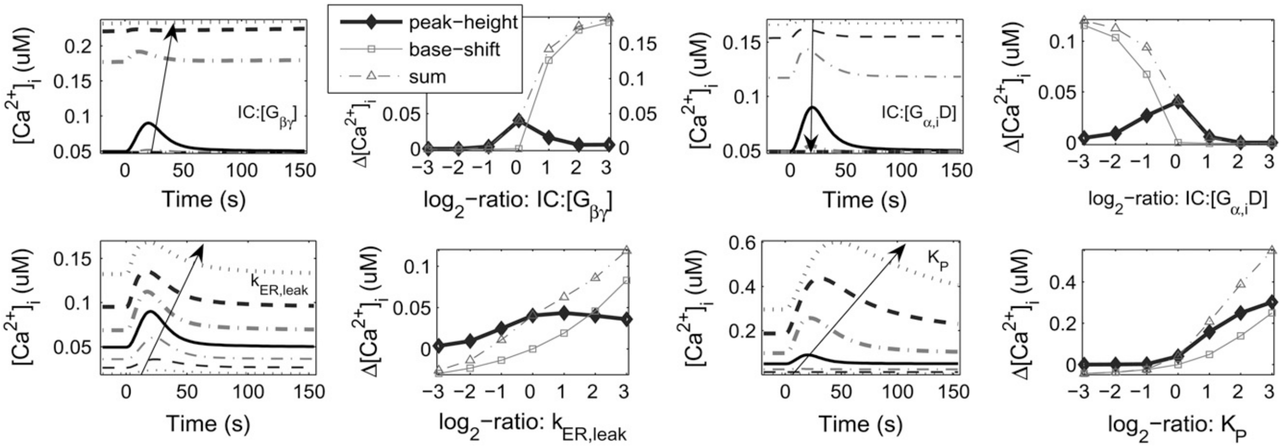

FIGURE 7 Temporal response, baseline shift, and peak height for perturbation in the parameters IC:[$G_{\beta\gamma}$], IC:[$G_{\alpha,i}D$], $k_{ER,leak}$, and K_P. For each parameter, two panels are used. The temporal response is shown in the left panel for which the *x* axis is labeled *time* (*s*). The baseline shift and peak height are shown in the right panel for which the *x* axis is labeled as *log*$_2$*-ratio*: ⟨*parameter name*⟩. The sum of baseline shift and peak height is also plotted in the right panels. In the left panel, the direction of increasing value of the parameter is shown.

further increase the peak height at higher doses. However, for the parameters resulting in decrease in the overall peak height, such as IC:[$G_{\alpha,i}D$] in Fig. 7 and K_{IP3} (not shown), a more interesting pattern of dose response is obtained. This is elucidated in Fig. 8 *A*, *panel 1*, which shows the dose-response surface for variations in IC:[R] and the C5a dose. Fig. 8, *panel 2* shows the dose response surface for variations in K_{IP3}. There appear to be three distinct regimes characterized by low K_{IP3} and high C5a dose (large peak); high K_{IP3} and high C5a dose (short peak); and low K_{IP3} and low C5a dose (medium peak). Similar behavior is obtained for perturbation in other parameters, depending upon their behavioral similarity to IC:[R] or K_{IP3}. Variation in IC:[R] does not affect the basal level, but a decrease in K_{IP3} leads to increased basal levels. These effects are visible at very low C5a in Fig. 8 *A*.

Global perturbation

Another type of perturbation involved simultaneous change in all rate-constant parameters such as forward and reverse rate constants, k_f and k_b, and enzymatic rate constants V_{max} and k_{cat}. Such parameters are listed in Table S9 (Supplementary Material). Parameters such as K_m and $Pr_{tot,e}$ were not changed. In one case, these parameters were increased twofold and in another decreased by 50% compared to their base values. Such a scenario is likely to occur, for instance, when the temperature of the system is altered. Fig. 8 *B*, *left* and *right*, shows the responses of [IP_3] and [Ca^{2+}]$_I$, respectively, in these scenarios. The relative baseline shift, as compared to the peak height without perturbation, is $<2\%$ for the [IP_3] response whereas for [Ca^{2+}]$_I$, it is 50% and -36% for increase and decrease, respectively. On the contrary, the peak-height, measured from the respective basal levels, varies between 19% and -15% for [IP_3] and between 11% and -6% for [Ca^{2+}]$_i$. Thus, the response of both [IP_3] and [Ca^{2+}]$_i$ is very robust for reasonable physiological variations. These results are consistent with those observed by Mishra and Bhalla (13). The time to reach the peak and then return to basal level is decreased (increased) with increased (decreased) values of the parameters.

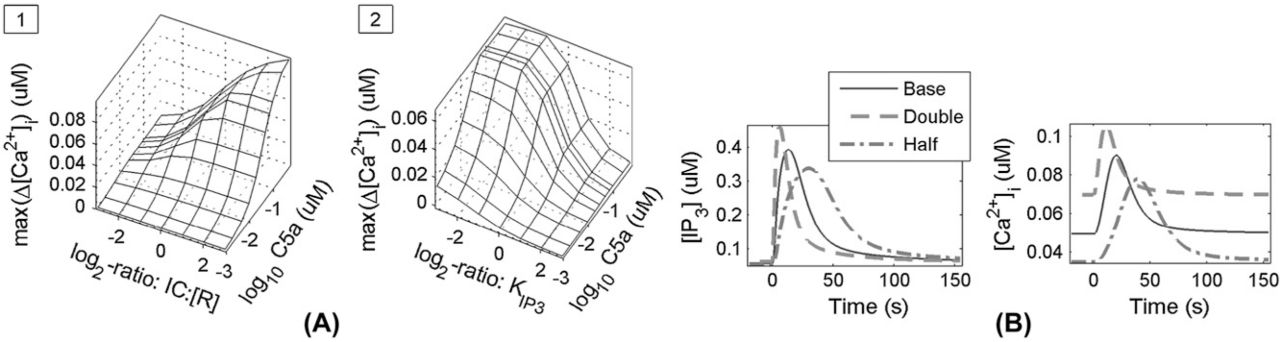

FIGURE 8 (*A*) Dose-response surface for variation in a chosen parameter and the C5a dose. (*1*) Surface for the parameter IC:[R]. (*2*) Surface for the parameter K_{IP3}. (*B*) Effect of simultaneous increase or decrease in all kinetic parameters. (*Left*) Response for [IP_3]. (*Right*) Response for [Ca^{2+}]$_i$.

DISCUSSION

We have developed a kinetic model to characterize the intracellular calcium dynamics in RAW 264.7 cells in response to the anaphylaxin C5a that activates PLCβ via the G-protein G_i upon binding to its receptor C5aR. The in vivo data from the AfCS allowed us to constrain the parameters within the ranges suggested by legacy knowledge and in other cell types. This was achieved through an optimization approach. It should be noted that in test simulations using the parameter values as presented in the literature, the experimental data could not be produced. This is not surprising because most of the mechanisms can be similar across different cell types, but the parameters can vary substantially not only across different cell types (13,21) but also across different subpopulations of cells. Thus, parameter constraining was essential. Further, as Mishra and Bhalla (13) have suggested, the parameters based on in vitro data can be different from those suitable for use with in vivo data. Interestingly, the optimized values of the parameters related to the IP_3R dynamics are quite close to their literature values (62). Our model, although it is coarse-grained and hence relatively simplistic, captures most of the mechanisms included in the models presented in the literature for nonexcitable cells and metabotropic receptors. The model is context-specific in that the mechanisms for the receptor and G-protein module are for the G-protein G_i, though they are easily extensible to other GTPase cycles. The EC_{50} value of C5a for the dose-response curve is about half of the total pool of surface receptors. We have included some mechanisms explicitly to facilitate quantitative modeling of the knockdown of many proteins, including GRK, $G_{\beta\gamma}$, $G_{\alpha,i}$, and PLCβ, on which in vivo data is available from AfCS. Besides incorporating the three-site model of IP_3 and Ca^{2+} binding to IP_3R (62,63) to demonstrate the CICR effect, interaction with the mitochondria and the ECM have also been modeled. Interaction with the ECM is important for knockdowns resulting in a baseline shift, e.g., the experimental data on knockdown of $G_{\alpha,i}$ (Table S3, *dataset 3*). The recent evidence about the presence of IP_3R channels on the plasma membrane provides further support for this effect (18,19,66,67).

Methodological novelty

The methodological novelty of this work is the ability to utilize multiple datasets exhibiting subpopulational variability, a biological fact of living cells, and in vivo data (69). Our approach reveals a challenge for both the experimentalists and the modelers alike in that none of them alone can handle it efficiently, since the number of parameters to be constrained increases linearly with the number of datasets to be used. This, essentially, leads to lesser constraining of the parameter space even though the ratio-based approach alleviates this effect. The success of this method is evident as all the four datasets used for constraining the parameters are predicted well in terms of basal levels, peak height, qualitative shape, and rise time. In fact, this approach has made it possible to resolve the anomalous observation on the response for the knockdown of PLCβ (dataset 4), as compared to the basal data (dataset 1).

Dose response

Dose response provides insights into the capacity of the cellular system and the local perturbation of the receptor-ligand binding system. The dose response predicted by our model agrees with those observed in the AfCS data within the subpopulational variability. The EC_{50} value of 18–20 nM is within the suggestive range of 5–20 nM. Since it has been observed that EC_{50} is about half of R_{tot} due to the 1:1 binding ratio of C5a/C5aR, R_{tot} can be computed using EC_{50} values obtained from carefully controlled experiments, serving as a soft sensor. The dose-response analysis has revealed that the peak response is dependent on the capacity of all the modules and, in general, is limited by the least-capacity module as the species in that module saturate first. The ultrasensitivity of the dose response is due to the multiple steps involved in the cascade from the receptor activation to calcium release from the ER and the saturation effect.

Multiparametric variability analysis and sensitivity analysis

Most parameters were constrained within an order of magnitude (Table S7). As much as half of the sensitive parameters are related to the production of IP_3, IP_3R channel kinetics, or other release and uptake mechanisms (Tables S7 and S8). These have been the focus of both theoretical (62,63) and experimental research in regard to the maintenance of the homeostasis of intracellular calcium (81,85,87) and its role in physiological effects such as neurological processes (88,89) and heartbeat (90). Thus, MPVA can serve as a useful heuristic to identify most of the sensitive parameters without carrying out local or large perturbations in the parameters separately. However, sensitivity analysis is also required as this approach complements the MPVA approach. Global sensitivity analysis has shown that the system is very robust to physiological perturbations such as small changes in temperature (13).

SUPPLEMENTARY MATERIAL

An online supplement to this article can be found by visiting BJ Online at http://www.biophysj.org.

The supporting document ''calcium_paper_Supplementary-part-1.pdf'' contains additional text, the Tables S1–9 and the Figures S1–2.

We acknowledge the Macrophage Biology Laboratory of the Alliance for Cellular Signaling (University of California, San Francisco) for the experimental data. We are grateful to the two anonymous reviewers for their insightful comments and suggestions. This research was supported by National Institutes of Health Collaborative Grants U54 GM62114 (Alliance for Cellular Signaling (S.S.)) and U54 GM69338-04 (LIPID Metabolites and Pathways Strategy (S.S.)), National Institutes of Health grant R01-GM068959 (S.S.), and a grant from the Hilblom foundation (S.S.).

REFERENCES

1. Carafoli, E. 2002. Calcium signaling: a tale for all seasons. *Proc. Natl. Acad. Sci. USA.* 99:1115–1122.
2. Karcher, R. L., J. T. Roland, F. Zappacosta, M. J. Huddleston, R. S. Annan, S. A. Carr, and V. I. Gelfand. 2001. Cell cycle regulation of myosin-V by calcium/calmodulin-dependent protein kinase II. *Science.* 293:1317–1320.
3. Bedard, K., E. Szabo, M. Michalak, and M. Opas. 2005. Cellular functions of endoplasmic reticulum chaperones calreticulin, calnexin, and ERp57. *Int. Rev. Cytol.* 245:91–121.
4. Johnson, S., M. Michalak, M. Opas, and P. Eggleton. 2001. The ins and outs of calreticulin: from the ER lumen to the extracellular space. *Trends Cell Biol.* 11:122–129.
5. Michalak, M., P. Mariani, and M. Opas. 1998. Calreticulin, a multifunctional Ca^{2+} binding chaperone of the endoplasmic reticulum. *Biochem. Cell Biol.* 76:779–785.
6. Kim, Y., J. S. Moon, K. S. Lee, S. Y. Park, J. Cheong, H. S. Kang, H. Y. Lee, and H. D. Kim. 2004. Ca^{2+}/calmodulin-dependent protein phosphatase calcineurin mediates the expression of iNOS through IKK and NF-kappaB activity in LPS-stimulated mouse peritoneal macrophages and RAW 264.7 cells. *Biochem. Biophys. Res. Commun.* 314: 695–703.
7. Berridge, M. J., M. D. Bootman, and H. L. Roderick. 2003. Calcium signalling: dynamics, homeostasis and remodelling. *Nat. Rev. Mol. Cell Biol.* 4:517–529.
8. Jafri, M. S., J. J. Rice, and R. L. Winslow. 1998. Cardiac Ca^{2+} dynamics: the roles of ryanodine receptor adaptation and sarcoplasmic reticulum load. *Biophys. J.* 74:1149–1168.
9. Puceat, M., and M. Jaconi. 2005. Ca^{2+} signalling in cardiogenesis. *Cell Calcium.* 38:383–389.
10. Greenstein, J. L., R. Hinch, and R. L. Winslow. 2006. Mechanisms of excitation-contraction coupling in an integrative model of the cardiac ventricular myocyte. *Biophys. J.* 90:77–91.
11. Greenstein, J. L., and R. L. Winslow. 2002. An integrative model of the cardiac ventricular myocyte incorporating local control of Ca^{2+} release. *Biophys. J.* 83:2918–2945.
12. Lemon, G., W. G. Gibson, and M. R. Bennett. 2003. Metabotropic receptor activation, desensitization and sequestration—I: modelling calcium and inositol 1,4,5-trisphosphate dynamics following receptor activation. *J. Theor. Biol.* 223:93–111.
13. Mishra, J., and U. S. Bhalla. 2002. Simulations of inositol phosphate metabolism and its interaction with InsP(3)-mediated calcium release. *Biophys. J.* 83:1298–1316.
14. Irvine, R. F. 2003. 20 years of Ins(1,4,5)P3, and 40 years before. *Nat. Rev. Mol. Cell Biol.* 4:586–590.
15. Berridge, M. J. 1990. Calcium oscillations. *J. Biol. Chem.* 265:9583–9586.
16. Berridge, M. J. 1992. Inositol trisphosphate and calcium oscillations. *Adv. Second Messenger Phosphoprotein Res.* 26:211–223.
17. Meyer, T., and L. Stryer. 1988. Molecular model for receptor-stimulated calcium spiking. *Proc. Natl. Acad. Sci. USA.* 85:5051–5055.
18. Dellis, O., S. G. Dedos, S. C. Tovey, R. Taufiq Ur, S. J. Dubel, and C. W. Taylor. 2006. Ca^{2+} entry through plasma membrane IP3 receptors. *Science.* 313:229–233.
19. Vig, M., C. Peinelt, A. Beck, D. L. Koomoa, D. Rabah, M. Koblan-Huberson, S. Kraft, H. Turner, A. Fleig, R. Penner, and J. P. Kinet. 2006. CRACM1 is a plasma membrane protein essential for store-operated Ca^{2+} entry. *Science.* 312:1220–1223.
20. Hofer, T., L. Venance, and C. Giaume. 2002. Control and plasticity of intercellular calcium waves in astrocytes: a modeling approach. *J. Neurosci.* 22:4850–4859.
21. Van Den Brink, G. R., S. M. Bloemers, B. Van Den Blink, L. G. Tertoolen, S. J. Van Deventer, and M. P. Peppelenbosch. 1999. Study of calcium signaling in non-excitable cells. *Microsc. Res. Tech.* 46: 418–433.
22. Takahashi, A., P. Camacho, J. D. Lechleiter, and B. Herman. 1999. Measurement of intracellular calcium. *Physiol. Rev.* 79:1089–1125.
23. AfCS (Alliance for Cellular Signaling) Protocols. http://www.signaling-gateway.org/data/ProtocolLinks.html. Accessed August 16, 2006.
24. Hinch, R. 2004. Stability of cardiac waves. *Bull. Math. Biol.* 66:1887–1908.
25. Hinch, R., J. L. Greenstein, A. J. Tanskanen, L. Xu, and R. L. Winslow. 2004. A simplified local control model of calcium-induced calcium release in cardiac ventricular myocytes. *Biophys. J.* 87:3723–3736.
26. Lemon, G., J. Brockhausen, G. H. Li, W. G. Gibson, and M. R. Bennett. 2005. Calcium mobilization and spontaneous transient outward current characteristics upon agonist activation of P2Y2 receptors in smooth muscle cells. *Biophys. J.* 88:1507–1523.
27. Doi, T., S. Kuroda, T. Michikawa, and M. Kawato. 2005. Inositol 1,4,5-trisphosphate-dependent Ca^{2+} threshold dynamics detect spike timing in cerebellar Purkinje cells. *J. Neurosci.* 25:950–961.
28. Shannon, T. R., F. Wang, and D. M. Bers. 2005. Regulation of cardiac sarcoplasmic reticulum Ca release by luminal [Ca] and altered gating assessed with a mathematical model. *Biophys. J.* 89:4096–4110.
29. The AfCS FXM signaling map. http://www.signaling-gateway.org/data/fxm/query?type=map. Accessed August 16, 2006.
30. Letari, O., S. Nicosia, C. Chiavaroli, P. Vacher, and W. Schlegel. 1991. Activation by bacterial lipopolysaccharide causes changes in the cytosolic free calcium concentration in single peritoneal macrophages. *J. Immunol.* 147:980–983.
31. Pinelli, E., B. Pipy, J. Teissie, and B. Gabriel. 2001. Calcium oscillations induced by lindane in peritoneal macrophages of mice: control by the maturation stage of the macrophage. *J. Soc. Biol.* 195:285–295.
32. Sauviat, M. P., and N. Pages. 2002. Cardiotoxicity of lindane, a gamma isomer of hexachlorocyclohexane. *J. Soc. Biol.* 196:339–348.
33. Chang, C. Y., K. R. Farrell, and R. C. Baker. 2000. Phosphatidylethanol stimulates calcium-dependent cytosolic phospholipase A(2) activity of a macrophage cell line (RAW 264.7). *J. Biomed. Sci.* 7: 311–316.
34. Wiesner, T. F., B. C. Berk, and R. M. Nerem. 1996. A mathematical model of cytosolic calcium dynamics in human umbilical vein endothelial cells. *Am. J. Physiol. Cell Physiol.* 39:C1556–C1569.
35. Fink, C. C., B. Slepchenko, I. I. Moraru, J. Watras, J. C. Schaff, and L. M. Loew. 2000. An image-based model of calcium waves in differentiated neuroblastoma cells. *Biophys. J.* 79:163–183.
36. Raser, J. M., and E. K. O'Shea. 2005. Noise in gene expression: origins, consequences, and control. *Science.* 309:2010–2013.
37. Leslie, R. G. Q. 1999. Complement Receptors. *In* Encyclopedia of Life Sciences. John Wiley & Sons, Chichester, UK. http://www.els.net, doi:10.1038/npg.els.0000512. 1–9.
38. Brown, E. J. 1992. Complement receptors, adhesion, and phagocytosis. *Infect. Agents Dis.* 1:63–70.
39. Janeway, C. A., P. Traver, M. Walport, and M. J. Shlomchik. 2005. Immunobiology: the immune system in health and disease. Garland Publishing, New York.
40. Greer, J. 1985. Model structure for the inflammatory protein C5a. *Science.* 228:1055–1060.
41. Huber-Lang, M. S., J. V. Sarma, S. R. McGuire, K. T. Lu, V. A. Padgaonkar, E. M. Younkin, R. F. Guo, C. H. Weber, E. R. Zuiderweg,

F. S. Zetoune, and P. A. Ward. 2003. Structure-function relationships of human C5a and C5aR. *J. Immunol.* 170:6115–6124.

42. March, D. R., L. M. Proctor, M. J. Stoermer, R. Sbaglia, G. Abbenante, R. C. Reid, T. M. Woodruff, K. Wadi, N. Paczkowski, J. D. Tyndall, S. M. Taylor, and D. P. Fairlie. 2004. Potent cyclic antagonists of the complement C5a receptor on human polymorphonuclear leukocytes. Relationships between structures and activity. *Mol. Pharmacol.* 65: 868–879.
43. Strachan, A. J., T. M. Woodruff, G. Haaima, D. P. Fairlie, and S. M. Taylor. 2000. A new small molecule C5a receptor antagonist inhibits the reverse-passive Arthus reaction and endotoxic shock in rats. *J. Immunol.* 164:6560–6565.
44. Mastellos, D., C. Andronis, A. Persidis, and J. D. Lambris. 2005. Novel biological networks modulated by complement. *Clin. Immunol.* 115:225–235.
45. The Alliance for Cellular Signaling (AfCS). http://www.signaling-gateway.org/. Accessed August 16, 2006.
46. Grynkiewicz, G., M. Poenie, and R. Y. Tsien. 1985. A new generation of Ca^{2+} indicators with greatly improved fluorescence properties. *J. Biol. Chem.* 260:3440–3450.
47. Henke, W., C. Cetinsoy, K. Jung, and S. Loening. 1996. Non-hyperbolic calcium calibration curve of fura-2: implications for the reliability of quantitative Ca^{2+} measurements. *Cell Calcium.* 20:287–292.
48. Hoffman, J. F., J. J. Linderman, and G. M. Omann. 1996. Receptor up-regulation, internalization, and interconverting receptor states. Critical components of a quantitative description of N-formyl peptide-receptor dynamics in the neutrophil. *J. Biol. Chem.* 271:18394–18404.
49. Riccobene, T. A., G. M. Omann, and J. J. Linderman. 1999. Modeling activation and desensitization of G-protein coupled receptors. Provides insight into ligand efficacy. *J. Theor. Biol.* 200:207–222.
50. Woolf, P. J., and J. J. Linderman. 2003. Untangling ligand induced activation and desensitization of G-protein-coupled receptors. *Biophys. J.* 84:3–13.
51. Yi, T. M., H. Kitano, and M. I. Simon. 2003. A quantitative characterization of the yeast heterotrimeric G protein cycle. *Proc. Natl. Acad. Sci. USA.* 100:10764–10769.
52. Wagner, J., and J. Keizer. 1994. Effects of rapid buffers on Ca^{2+} diffusion and Ca^{2+} oscillations. *Biophys. J.* 67:447–456.
53. Fushman, D., T. Najmabadi-Haske, S. Cahill, J. Zheng, H. LeVine 3rd, and D. Cowburn. 1998. The solution structure and dynamics of the pleckstrin homology domain of G protein-coupled receptor kinase 2 (β-adrenergic receptor kinase 1). A binding partner of $G_{\beta\gamma}$subunits. *J. Biol. Chem.* 273:2835–2843.
54. Yang, X. L., Y. L. Zhang, Z. S. Lai, F. Y. Xing, and Y. H. Liu. 2003. Pleckstrin homology domain of G protein-coupled receptor kinase-2 binds to PKC and affects the activity of PKC kinase. *World J. Gastroenterol.* 9:800–803.
55. Christophe, T., M. J. Rabiet, M. Tardif, M. D. Milcent, and F. Boulay. 2000. Human complement 5a (C5a) anaphylatoxin receptor (CD88) phosphorylation sites and their specific role in receptor phosphorylation and attenuation of G protein-mediated responses. Desensitization of C5a receptor controls superoxide production but not receptor sequestration in HL-60 cells. *J. Biol. Chem.* 275:1656–1664.
56. Sitaramayya, A., and N. W. Bunnett. 1999. Cell surface receptors: mechanisms of signaling and activation. *In* Introduction to Cellular Signal Transduction. A. Sitaramayya, editor. Birkhauser, Boston. 7–28.
57. Elenko, E., T. Fischer, I. Niesman, T. Harding, T. McQuistan, M. Von Zastrow, and M. G. Farquhar. 2003. Spatial regulation of $G_{\alpha i}$ protein signaling in clathrin-coated membrane microdomains containing GAIP. *Mol. Pharmacol.* 64:11–20.
58. Bornheimer, S. J., M. R. Maurya, M. G. Farquhar, and S. Subramaniam. 2004. Computational modeling reveals how interplay between components of a GTPase-cycle module regulates signal transduction. *Proc. Natl. Acad. Sci. USA.* 101:15899–15904.
59. Marhl, M., T. Haberichter, M. Brumen, and R. Heinrich. 2000. Complex calcium oscillations and the role of mitochondria and cytosolic proteins. *Biosystems.* 57:75–86.
60. Voronina, E., and G. M. Wessel. 2004. $\beta\gamma$ subunits of heterotrimeric G-proteins contribute to Ca^{2+} release at fertilization in the sea urchin. *J. Cell Sci.* 117:5995–6005.
61. Schuster, S., M. Marhl, and T. Hofer. 2002. Modeling of simple and complex calcium oscillations, from single-cell responses to intercellular signaling. *Eur. J. Biochem.* 269:1333–1355.
62. De Young, G. W., and J. Keizer. 1992. A single-pool inositol 1,4,5-trisphosphate-receptor-based model for agonist-stimulated oscillations in Ca^{2+} concentration. *Proc. Natl. Acad. Sci. USA.* 89:9895–9899.
63. Li, Y. X., and J. Rinzel. 1994. Equations for InsP3 receptor-mediated $[Ca^{2+}]$i oscillations derived from a detailed kinetic model: a Hodgkin-Huxley like formalism. *J. Theor. Biol.* 166:461–473.
64. Gill, D. L., and S. H. Chueh. 1985. An intracellular (ATP + Mg^{2+})-dependent calcium pump within the N1E–115 neuronal cell line. *J. Biol. Chem.* 260:9289–9297.
65. Lytton, J., M. Westlin, S. E. Burk, G. E. Shull, and D. H. MacLennan. 1992. Functional comparisons between isoforms of the sarcoplasmic or endoplasmic reticulum family of calcium pumps. *J. Biol. Chem.* 267: 14483–14489.
66. Feske, S., Y. Gwack, M. Prakriya, S. Srikanth, S. H. Puppel, B. Tanasa, P. G. Hogan, R. S. Lewis, M. Daly, and A. Rao. 2006. A mutation in Orai1 causes immune deficiency by abrogating CRAC channel function. *Nature.* 441:179–185.
67. Gill, D. L., M. A. Spassova, and J. Soboloff. 2006. Signal transduction. Calcium entry signals–trickles and torrents. *Science.* 313:183–184.
68. Haberichter, T., M. Marhl, and R. Heinrich. 2001. Birhythmicity, trirhythmicity and chaos in bursting calcium oscillations. *Biophys. Chem.* 90:17–30.
69. Babnigg, G., B. Heller, and M. L. Villereal. 2000. Cell-to-cell variation in store-operated calcium entry in HEK-293 cells and its impact on the interpretation of data from stable clones expressing exogenous calcium channels. *Cell Calcium.* 27:61–73.
70. Pumiglia, K. M., H. LeVine, T. Haske, T. Habib, R. Jove, and S. J. Decker. 1995. A direct interaction between G-protein $\beta\gamma$ subunits and the Raf-1 protein kinase. *J. Biol. Chem.* 270:14251–14254.
71. Chen, S., B. D. Spiegelberg, F. Lin, E. J. Dell, and H. E. Hamm. 2004. Interaction of $G_{\beta\gamma}$ with RACK1 and other WD40 repeat proteins. *J. Mol. Cell. Cardiol.* 37:399–406.
72. Chen, W., X. R. Ren, C. D. Nelson, L. S. Barak, J. K. Chen, P. A. Beachy, F. de Sauvage, and R. J. Lefkowitz. 2004. Activity-dependent internalization of smoothened mediated by β-arrestin 2 and GRK2. *Science.* 306:2257–2260.
73. Daaka, Y., J. A. Pitcher, M. Richardson, R. H. Stoffel, J. D. Robishaw, and R. J. Lefkowitz. 1997. Receptor and G $\beta\gamma$ isoform-specific interactions with G protein-coupled receptor kinases. *Proc. Natl. Acad. Sci. USA.* 94:2180–2185.
74. Sklar, L. A., P. A. Hyslop, Z. G. Oades, G. M. Omann, A. J. Jesaitis, R. G. Painter, and C. G. Cochrane. 1985. Signal transduction and ligand-receptor dynamics in the human neutrophil. Transient responses and occupancy-response relations at the formyl peptide receptor. *J. Biol. Chem.* 260:11461–11467.
75. Sklar, L. A., and Z. G. Oades. 1985. Signal transduction and ligand-receptor dynamics in the neutrophil. Ca^{2+} modulation and restoration. *J. Biol. Chem.* 260:11468–11475.
76. Ross, E. M., and T. M. Wilkie. 2000. GTPase-activating proteins for heterotrimeric G proteins: regulators of G protein signaling (RGS) and RGS-like proteins. *Annu. Rev. Biochem.* 69:795–827.
77. Biddlecome, G. H., G. Berstein, and E. M. Ross. 1996. Regulation of phospholipase C-β1 by $G(q)$ and m1 muscarinic cholinergic receptor. Steady-state balance of receptor-mediated activation and GTPase-activating protein-promoted deactivation. *J. Biol. Chem.* 271:7999–8007.
78. Sprang, S. R. 1997. G protein mechanisms: insights from structural analysis. *Annu. Rev. Biochem.* 66:639–678.
79. Gilman, A. G. 1987. G-proteins, Transducers of receptor-generated signals. *Annu. Rev. Biochem.* 56:615–649.

80. Maurya, M. R., S. J. Bornheimer, V. Venkatasubramanian, and S. Subramaniam. 2005. Reduced-order modeling of biochemical networks: application to the GTPase-cycle signaling module. *IEE Syst. Biol.* 152:229–242.

81. Espelt, M. V., A. Y. Estevez, X. Yin, and K. Strange. 2005. Oscillatory Ca^{2+} signaling in the isolated *Caenorhabditis elegans* intestine: role of the inositol-1,4,5-trisphosphate receptor and phospholipases C β and γ. *J. Gen. Physiol.* 126:379–392.

82. Frecker, H., S. Munk, H. Wang, and C. Whiteside. 2005. Mesangial cell-reduced Ca^{2+} signaling in high glucose is due to inactivation of phospholipase C-β3 by protein kinase C. *Am. J. Physiol. Renal Physiol.* 289:F1078–F1087.

83. Higgins, E. R., M. B. Cannell, and J. Sneyd. 2006. A buffering SERCA pump in models of calcium dynamics. *Biophys. J.* 91:151–163.

84. Hwang, J. I., H. S. Kim, J. R. Lee, E. Kim, S. H. Ryu, and P. G. Suh. 2005. The interaction of phospholipase C-β3 with Shank2 regulates mGluR-mediated calcium signal. *J. Biol. Chem.* 280:12467–12473.

85. Hwang, J. I., K. J. Shin, Y. S. Oh, J. W. Choi, Z. W. Lee, D. Kim, K. S. Ha, H. S. Shin, S. H. Ryu, and P. G. Suh. 2005. Phospholipase C-β3 mediates the thrombin-induced Ca^{2+} response in glial cells. *Mol. Cells.* 19:375–381.

86. Redondo, P. C., J. A. Rosado, J. A. Pariente, and G. M. Salido. 2005. Collaborative effect of SERCA and PMCA in cytosolic calcium homeostasis in human platelets. *J. Physiol. Biochem.* 61:507–516.

87. Zhang, S. L., A. V. Yeromin, X. H. Zhang, Y. Yu, O. Safrina, A. Penna, J. Roos, K. A. Stauderman, and M. D. Cahalan. 2006. Genome-wide RNAi screen of Ca^{2+} influx identifies genes that regulate Ca^{2+} release-activated Ca^{2+} channel activity. *Proc. Natl. Acad. Sci. USA.* 103:9357–9362.

88. Ruiz de Azua, I., E. Del Olmo, A. Pazos, and J. Salles. 2006. Transmembrane signaling through phospholipase C-β in the developing human prefrontal cortex. *J. Neurosci. Res.* 84:13–26.

89. Nakamura, M., K. Sato, M. Fukaya, K. Araishi, A. Aiba, M. Kano, and M. Watanabe. 2004. Signaling complex formation of phospholipase Cβ4 with metabotropic glutamate receptor type 1α and 1,4,5-trisphosphate receptor at the perisynapse and endoplasmic reticulum in the mouse brain. *Eur. J. Neurosci.* 20:2929–2944.

90. Misquitta, C. M., D. P. Mack, and A. K. Grover. 1999. Sarco/endoplasmic reticulum Ca^{2+} (SERCA)-pumps: link to heart beats and calcium waves. *Cell Calcium.* 25:277–290.